

Quantifying Intrinsic and Extrinsic Contributions to Seismic Anisotropy in Tomographic Models

John Keith Magali¹, Thomas Bodin¹, Navid Hedjazian¹, Yanick Ricard¹, Yann Capdeville², and Eric Debayle¹

¹Univ Lyon, Univ Lyon 1, ENSL, UJM-Saint-Etienne, CNRS, LGL-TPE, F-69622, Villeurbanne, France

²Laboratoire de Planétologie et Géodynamique, CNRS, UMR 6112, Université de Nantes, F-44322, Nantes, Cedex 3, France.

November 23, 2022

Abstract

Seismic anisotropy in the Earth's mantle inferred from seismic observations is usually interpreted either in terms of intrinsic anisotropy due to Crystallographic Preferred Orientation (CPO) of minerals, or extrinsic anisotropy due to rock-scale Shape Preferred Orientation (SPO). The coexistence of both contributions misconstrues the origins of seismic anisotropy observed in seismic tomography models. It is thus essential to discriminate CPO from SPO. Homogenization/upscaling theory provides means to achieve this goal. This theory enables to compute the effective elastic properties of a heterogeneous medium, as seen by long-period waves. In this work, we investigate the effects of upscaling an intrinsically anisotropic and highly heterogeneous Earth's mantle. We show analytically in 1-D that the full effective radial anisotropy ξ^* is approximately the product of the effective intrinsic radial anisotropy ξ^* CPO and the extrinsic radial anisotropy ξ^* SPO : $\xi^* = \xi^* \text{CPO} \times \xi^* \text{SPO}$. This law is verified numerically in the case of a 2-D marble cake model of the mantle with a binary composition, and in the presence of CPO obtained from a micro-mechanical model of olivine deformation. We compute the long-wavelength effective equivalent of this mantle model using the 3-D non-periodic elastic homogenization technique. Our numerical findings predict that for wavelenghts smaller than the scale of deformation patterns, tomography may overestimate the true anisotropy (i.e. intrinsic anisotropy due to CPO) due to significant SPO-induced extrinsic anisotropy. However, at wavelenghts larger than deformation patterns, intrinsic anisotropy is always underestimated in tomographic models due to the spatial averaging of the preferred orientation of anisotropic minerals. Thus, we show that it is imperative to homogenize a CPO evolution model first before drawing comparisons with tomographic models. As a demonstration, we use our composite law with a homogenized CPO model of a plate-driven flow underneath a mid-ocean ridge, to estimate the SPO contribution to an existing tomographic model of radial anisotropy.

Quantifying Intrinsic and Extrinsic Contributions to Seismic Anisotropy in Tomographic Models

J. K. Magali¹, T. Bodin¹, N. Hedjazian¹, Y. Ricard¹, Y. Capdeville², E. Debayle¹

¹Univ Lyon, Univ Lyon 1, ENSL, UJM-Saint-Etienne, CNRS, LGL-TPE, F-69622, Villeurbanne, France

²Laboratoire de Planétologie et Géodynamique, CNRS, UMR 6112, Université de Nantes, F-44322

Nantes, Cedex 3, France.

Key Points:

- We propose a theoretical expression that relates the observed seismic anisotropy to its intrinsic and extrinsic contributions.
- For wavelengths longer than the scale of deformation patterns in the mantle, we show that observed anisotropy in tomographic models underestimates intrinsic anisotropy, due to the spatial averaging of intrinsic anisotropy over long wavelengths.
- For wavelengths shorter than the scale of deformation patterns, observed anisotropy overestimates intrinsic anisotropy due to the presence of extrinsic anisotropy.

Abstract

Seismic anisotropy in the Earth’s mantle inferred from seismic observations is usually interpreted either in terms of intrinsic anisotropy due to Crystallographic Preferred Orientation (CPO) of minerals, or extrinsic anisotropy due to rock-scale Shape Preferred Orientation (SPO). The coexistence of both contributions misconstrues the origins of seismic anisotropy observed in seismic tomography models. It is thus essential to discriminate CPO from SPO. Homogenization/upscaling theory provides means to achieve this goal. This theory enables to compute the effective elastic properties of a heterogeneous medium, as seen by long-period waves. In this work, we investigate the effects of upscaling an intrinsically anisotropic and highly heterogeneous Earth’s mantle. We show analytically in 1-D that the full effective radial anisotropy ξ^* is approximately the product of the effective intrinsic radial anisotropy ξ_{CPO}^* and the extrinsic radial anisotropy ξ_{SPO}^* :

$$\xi^* \approx \xi_{\text{CPO}}^* \times \xi_{\text{SPO}}^*.$$

This law is verified numerically in the case of a 2-D marble cake model of the mantle with a binary composition, and in the presence of CPO obtained from a micro-mechanical model of olivine deformation. We compute the long-wavelength effective equivalent of this mantle model using the 3-D non-periodic elastic homogenization technique. Our numerical findings predict that for wavelengths smaller than the scale of deformation patterns, tomography may over-estimate the true anisotropy (*i.e.* intrinsic anisotropy due to CPO) due to significant SPO-induced extrinsic anisotropy. However, at wavelengths larger than deformation patterns, intrinsic anisotropy is always underestimated in tomographic models due to the spatial averaging of the preferred orientation of anisotropic minerals. Thus, we show that it is imperative to homogenize a CPO evolution model first before drawing comparisons with tomographic models. As a demonstration, we use our composite law with a homogenized CPO model of a plate-driven flow underneath a mid-ocean ridge, to estimate the SPO contribution to an existing tomographic model of radial anisotropy.

1 Introduction

Seismic anisotropy in the Earth’s mantle originates from various processes and can be observed at different spatial scales (Hansen et al., 2021). At the mineral scale, crystallographic preferred orientation (CPO) of anisotropic mantle minerals due

49 to progressive shearing over time produces large-scale intrinsic anisotropy (Nicolas
 50 & Christensen, 1987; Maupin & Park, 2015). On the other hand, rock-scale shape
 51 preferred orientation (SPO) such as layered heterogeneous materials, seismic disconti-
 52 nuities, preferentially-oriented cracks or conduits containing fluid intrusions unresolved
 53 by long period seismic waves are mapped as large-scale extrinsic anisotropy (Backus,
 54 1962; Crampin & Booth, 1985).

55 Although these two mechanisms are completely different, a medium may be ei-
 56 ther (or both) intrinsically anisotropic and extrinsically anisotropic at a given scale,
 57 depending on the minimum wavelength of the observed wavefield used (Maupin et al.,
 58 2007; Wang et al., 2013; Fichtner et al., 2013; Bodin et al., 2015). Backus (1962)
 59 showed that a horizontally-layered isotropic medium is equivalent to a homogeneous
 60 radially anisotropic medium with a vertical axis of symmetry when sampled by seismic
 61 waves whose wavelength is much longer than the thickness of layers. This urged seis-
 62 mologists to interpret tomographic models separately depending on the type of data
 63 used (*i.e.*, different data-types sample different length scales). Scattering studies use
 64 high frequency body waves and interpret small-scale isotropic heterogeneities in terms
 65 of phase changes (e.g. Tauzin & Ricard, 2014) or chemical stratification (e.g. Tauzin
 66 et al., 2016). On the other hand, long period surface waves with typical wavelengths of
 67 the order 10^2 km retrieve a smooth anisotropic mantle with scales consistent with con-
 68 vective flow (e.g. Debayle & Ricard, 2013; Bodin et al., 2015; Maupin & Park, 2015).
 69 Surface waves however lack the resolving power to recover sharp seismic discontinuities
 70 and instead, map these as long wavelength radial anisotropy (Backus, 1962; Capdev-
 71 ille et al., 2013). Anisotropic structures retrieved from tomography may therefore be
 72 a combination of apparent extrinsic anisotropy due to SPO and deformation-induced
 73 intrinsic anisotropy. The ambiguity on the origin of observed anisotropy (*i.e.* whether
 74 a material is intrinsically anisotropic or strongly heterogeneous) may mislead seismolo-
 75 gists in interpreting the structural origin of seismic anisotropy observed in tomographic
 76 images.

77 **1.1 Intrinsic anisotropy due to Crystallographic Preferred Orientation**

78 Intrinsic anisotropy results from the preferred alignment of anisotropic crystals
 79 in an aggregate when subjected to a macroscopic deformation. In the mantle, single
 80 crystal olivine exhibits orthorhombicity, and hence suffers variations in fast and slow

81 P- and S-wave velocities up to 20 % (Kumazawa & Anderson, 1969). When olivine
82 and pyroxene form a polycrystalline aggregate and are subsequently deformed in the
83 mantle flow, their CPO can be described in terms of a hexagonally symmetric medium
84 (e.g. J. Montagner & Nataf, 1988).

85 Observations of large-scale anisotropy in tomographic models appear to be ubiq-
86 uitous in regions associated with strong deformation, and have often been interpreted
87 in terms of convective flow (McKenzie, 1979). For instance, tomographic imaging
88 has revealed the presence of positive radial anisotropy (*i.e.*, horizontally propagating
89 SH -waves traveling faster than SV -waves) of about 4% in the upper ~ 250 km of
90 the mantle and has been interpreted as lateral flow (refer to Long and Becker (2010)
91 for a comprehensive review). Long wavelength seismic anisotropy is also prevalent
92 in the transition zone (e.g. Trampert & van Heijst, 2002; Wookey & Kendall, 2004)
93 although its origin is still highly debated (Chen & Brudzinski, 2003; Chang & Fer-
94 reira, 2019; Sturgeon et al., 2019). Probing deeper depths, the lower mantle appears
95 to be isotropic (e.g. Meade et al., 1995) barring the D" layer where enough evidence
96 have shown it to be anisotropic (e.g. Kendall & Silver, 1998; McNamara et al., 2002;
97 Panning & Romanowicz, 2006).

98 Since CPO maps the deformation patterns, CPO may deviate from the flow
99 direction. This is because the deformation patterns relate not to the velocity field itself,
100 but to the velocity gradient. Moreover, CPO is not instantaneous, but depends on the
101 history of the deformation. As a result, regions with short deformation trajectories
102 such as beneath mid-ocean ridges appear to have under-developed CPO, and would
103 lag behind the direction of shear deformation (É. Kaminski & Ribe, 2002).

104 Based on laboratory experiments of simple shear, the fast axis of olivine tends
105 to align parallel to the long axis of the finite strain ellipsoid (FSE) at low strains due
106 to plastic deformation (Zhang & Karato, 1995). At larger strains, dynamic recryst-
107 tallization facilitates the alignment of the olivine fast axis towards the direction of
108 shear (Zhang & Karato, 1995; Bystricky et al., 2000). Mechanical models of CPO
109 evolution, coupled with geodynamic flow modeling have been developed to replicate
110 these results and have been extrapolated at scales consistent with mantle deformation
111 patterns. Among these is the viscoplastic self-consistent (VPSC) model which is used
112 to explain the mechanical response of polycrystals to plastic deformation (Tommasi et

113 al., 2000). Such tools however are computationally expensive, especially when applied
114 to 3-D and non-steady state flows (Lev & Hager, 2008). Another well-received method
115 is the D-Rex model, that utilizes a simple kinematic approach (E. Kaminski et al.,
116 2004). The predicted CPO is then converted to an elastic medium in which seismic
117 waves can propagate, and may explain anisotropic signatures observed in seismic data
118 recorded at the surface.

119 **1.2 Extrinsic anisotropy due to Shape Preferred Orientation**

120 Extrinsic anisotropy is observed under two conditions: (1) when the scale of the
121 heterogeneities is much smaller than the minimum wavelength of the observed wave-
122 field, and (2) when the contrast between seismic wave velocities (*i.e.* the amplitude of
123 heterogeneities) is large.

124 One of the known configurations at which extrinsic anisotropy is produced is rock-
125 scale shape preferred orientation (SPO). In the Earth’s mantle, rock-scale SPO can
126 be the result of igneous differentiation, or more generally of the stirring of chemical
127 heterogeneities by tectonic or convective deformation (e.g. Faccenda et al., 2019).
128 Since magmatically differentiated oceanic lithosphere is composed of a basaltic crustal
129 layer blanketed by a depleted harzburgitic mantle (Allègre & Turcotte, 1986), mantle
130 structure is often modeled in terms of a mechanical mixture of these two end-member
131 compositions (e.g. Hofmann, 1988; Xu et al., 2008; Ballmer et al., 2015).

132 Large-scale thermal convection in the mantle triggers the constant injection of
133 oceanic lithosphere into the mantle (Coltice & Ricard, 1999). It then mechanically
134 stirs with the surrounding mantle and experiences a series of stretching and thinning
135 due to the normal and shear strains associated with convection (Allègre & Turcotte,
136 1986). This led Allègre and Turcotte (1986) to develop a geodynamic model of the
137 mantle that would depict marble cake-like patterns. In their model, the layering may
138 be erased either by dissolution processes when the stripes become thin enough that
139 chemical diffusion becomes efficient, or by mantle reprocessing at mid-ocean ridges.
140 Assuming that the mixing preserves the physical properties of the two-end members
141 with depth and over geological time scales, such processes may explain rock-scale seis-
142 mic heterogeneities observed in the mantle in agreement with the spectrum of isotropic

143 anomalies observed along ridges (Agranier et al., 2005; Xu et al., 2008; Stixrude &
144 Jeanloz, 2015).

145 In this paper, we extend the work of Alder et al. (2017) by estimating the long-
146 wavelength effective equivalent of a marble cake mantle as hypothesized by Allègre
147 and Turcotte (1986), but in the presence of intrinsic anisotropy. Our aim is to quan-
148 tify the level of effective anisotropy resulting from elastic homogenization, that is, the
149 relegated version of the true Earth as seen by long-wavelength seismic tomography.
150 Section 2 is a brief overview of the homogenization theory and provides a definition of
151 some terms and notations to guide the reader throughout the paper. Section 3 shows
152 1-D analytical expressions for homogenization and highlights a composite law that
153 separates intrinsic and extrinsic anisotropy for a layered and anisotropic media. Here,
154 we demonstrate that the effective anisotropy varies with the square of isotropic het-
155 erogeneities, as well as with the square of anisotropic heterogeneities, plus a cross term
156 related to their coupling. In section 4, we build a 2-D media analogous to the marble
157 cake model where we consider a mechanical mixture of two end-member compositions.
158 We follow this by introducing intrinsic anisotropy due to mantle deformation associ-
159 ated with convection patterns consistent with the marble cake model. We compute
160 the long-wavelength effective equivalent of the 2-D models using the Fast-Fourier Ho-
161 mogenization algorithm (Capdeville et al., 2015). Section 5 presents the results of the
162 previous section: one of the major findings is that in the absence of isotropic het-
163 erogeneities, intrinsic anisotropy is always underestimated upon homogenization due
164 to the spatial averaging of the preferred orientation of the anisotropic minerals. We
165 also verify numerically that the composite law derived in section 3 can be extended
166 to 2-D media. Finally in section 6, we apply the composite law to infer the extrinsic
167 component of anisotropy from a tomographic model of the upper-mantle beneath a
168 mid-ocean ridge with the help of a homogenized CPO model.

169 **2 Elastic homogenization**

170 Seismic tomography is only able to recover a smooth representation of the real
171 Earth due to the limited frequency band of seismic data. This smooth average, how-
172 ever, is not just a simple spatial average but is produced from highly non-linear up-
173 scaling relations. In the context of wave propagation, such upscaling relations, also
174 known as elastic homogenization, remove seismic heterogeneities whose scales are much

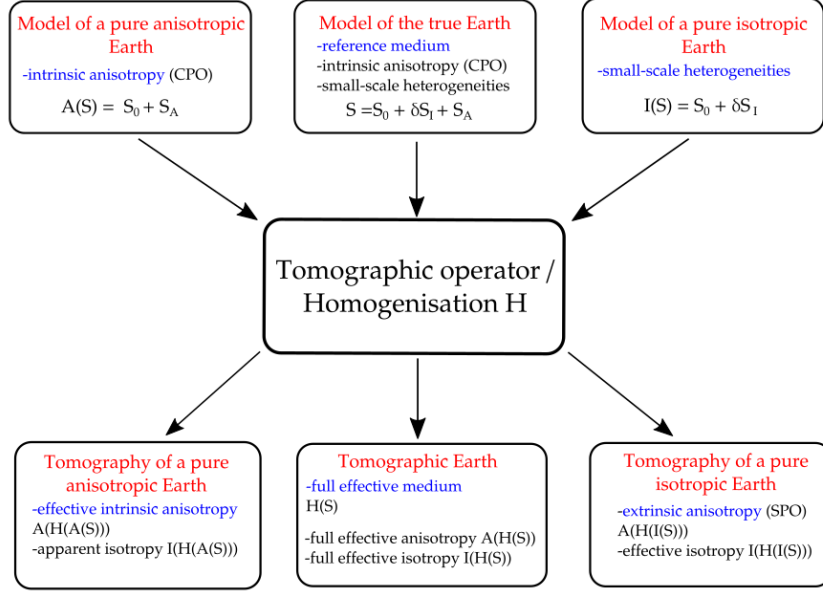


Figure 1. Homogenization of different Earth models and their respective outputs. The true Earth mantle (top middle box) is described by an average isotropic model S_0 , isotropic heterogeneities, δS_I and intrinsic anisotropy S_A , the sum of which being the elastic model S that tomography tries to recover. However, tomographic methods have only access to a homogenized model $H(S)$ (or full effective medium). This model has both isotropic components symbolized by $I(H(S))$ and anisotropic components, $A(H(S))$. The goal of this paper is to quantify the differences between $A(H(S))$ and $A(S)$, $I(H(S))$ and $I(S)$. Numerically we can also discuss how an anisotropic model without isotropic heterogeneities (boxes on the left) can be recovered and if the tomographic inversion can lead to apparent isotropic heterogeneities. Reciprocally (boxes on the right), one can quantify how much a pure isotropic model is recovered by the tomographic inversion and what is the level of extrinsic anisotropy (SPO) that can be estimated.

175 smaller than the minimum wavelength of the observed wavefield, and instead replace
 176 them with effective properties.

177 Hereafter, what we refer to as the *reference medium* $\mathbf{S}(\mathbf{r})$ is an elastic model of the
 178 real Earth varying in space \mathbf{r} that accounts for both intrinsic anisotropy due to CPO
 179 and small-scale isotropic heterogeneities that resemble marble cake-like patterns. This
 180 reference medium can be treated as a sum of several decompositions resulting from a
 181 cascade of orthogonal projections (Browaeys & Chevrot, 2004). One can then express
 182 $\mathbf{S}(\mathbf{r})$ in terms of an isotropic tensor $\mathbf{S}_I(\mathbf{r})$ plus an intrinsically anisotropic component
 183 $\mathbf{S}_A(\mathbf{r})$ related to CPO:

$$184 \quad \mathbf{S}(\mathbf{r}) = \mathbf{S}_I(\mathbf{r}) + \mathbf{S}_A(\mathbf{r}), \quad (1)$$

185 where $\mathbf{S}_I(\mathbf{r})$ can be decomposed further into:

$$186 \quad \mathbf{S}_I(\mathbf{r}) = \mathbf{S}_0 + \delta\mathbf{S}_I(\mathbf{r}). \quad (2)$$

187 Here, \mathbf{S}_0 is an isotropic tensor uniform in space, and $\delta\mathbf{S}_I(\mathbf{r})$ is a deviation from \mathbf{S}_0
 188 related to small-scale isotropic heterogeneities. The reference medium becomes:

$$189 \quad \mathbf{S}(\mathbf{r}) = \mathbf{S}_0 + \delta\mathbf{S}_I(\mathbf{r}) + \mathbf{S}_A(\mathbf{r}). \quad (3)$$

190 For convenience, let us introduce an operator \mathcal{I} that extracts the isotropic component
 191 from \mathbf{S} , and an operator \mathcal{A} that extracts the anisotropic component from \mathbf{S} :

$$192 \quad \begin{aligned} \mathcal{I}(\mathbf{S}(\mathbf{r})) &= \mathbf{S}_I(\mathbf{r}) \\ \mathcal{A}(\mathbf{S}(\mathbf{r})) &= \mathbf{S}_0 + \mathbf{S}_A(\mathbf{r}). \end{aligned} \quad (4)$$

193 These notations will be used heavily in the rest of the text to denote the isotropic
 194 and anisotropic components of an elastic medium. Radial anisotropy, in particular,
 195 quantifies the level of anisotropy when the medium is averaged azimuthally (J.-P. Mon-
 196 tagner, 2007; Maupin et al., 2007). In such a vertically transverse isotropic medium
 197 (VTI), the level of radial anisotropy is given by $(V_{SH}/V_{SV})^2$, where V_{SV} is the ve-
 198 locity of vertically traveling S waves or horizontally traveling S waves with vertical
 199 polarization, and V_{SH} is the velocity of horizontally traveling S waves with horizontal
 200 polarization. The *intrinsic radial anisotropy* associated with $\mathcal{A}(\mathbf{S})$ (*i.e.* due to the
 201 component \mathbf{S}_A) will be denoted by ξ_{CPO} .

202 In the event where long-period waves sample this reference medium, small-scale
 203 heterogeneities are seen only through their effective properties. Computing these ef-
 204 fective properties is designated by a mathematical operator \mathcal{H} called *upscaling* or

205 *homogenization*. Setting aside the imperfections of inversion algorithms and data cov-
 206 erage, performing seismic tomography can be viewed as applying the operator \mathcal{H} that
 207 homogenizes \mathbf{S} . The seismic tomography model/long-wavelength effective medium of
 208 \mathbf{S} is then $\mathcal{H}(\mathbf{S}) = \mathcal{H}(\mathbf{S}_0 + \delta\mathbf{S}_I + \mathbf{S}_A)$ which we now refer to as the *full effective medium*.
 209 The anisotropic component of the full effective medium given by $\mathcal{A}(\mathcal{H}(\mathbf{S}))$ will be re-
 210 ferred hereafter as the *full effective anisotropy* and its isotropic component $\mathcal{I}(\mathcal{H}(\mathbf{S}))$ is
 211 the *full effective isotropy*. We will symbolize the *full effective radial anisotropy* corre-
 212 sponding to $\mathcal{A}(\mathcal{H}(\mathbf{S}))$ with ξ^* .

213 On the other hand, the homogenized counterpart of a pure anisotropic Earth
 214 (*i.e.*, a model where only the anisotropic component varies spatially) is $\mathcal{H}(\mathcal{A}(\mathbf{S})) =$
 215 $\mathcal{H}(\mathbf{S}_0 + \mathbf{S}_A)$ where $\mathcal{A}(\mathcal{H}(\mathcal{A}(\mathbf{S})))$ is the *effective intrinsic anisotropy*. The *effective*
 216 *intrinsic radial anisotropy* corresponding to $\mathcal{A}(\mathcal{H}(\mathcal{A}(\mathbf{S})))$ will then be designated as
 217 ξ_{CPO}^* . Note that due to the non-linearity of \mathcal{H} , homogenization creates apparent
 218 isotropic heterogeneities in the elastic tensor $\mathcal{I}(\mathcal{H}(\mathcal{A}(\mathbf{S})))$ as a byproduct, albeit of low
 219 amplitude.

220 Finally, the tomographic counterpart of a pure isotropic Earth (*i.e.*, a model
 221 where the isotropic component varies spatially, and the anisotropic component is zero)
 222 is $\mathcal{H}(\mathcal{I}(\mathbf{S})) = \mathcal{H}(\mathbf{S}_0 + \delta\mathbf{S}_I)$ where the non-negligible apparent anisotropic compo-
 223 nent due to SPO $\mathcal{A}(\mathcal{H}(\mathcal{I}(\mathbf{S})))$ is called *extrinsic anisotropy*. Here, *extrinsic radial*
 224 *anisotropy* will be denoted by ξ_{SPO}^* (Refer to Figure 1 for a comprehensive summary).

225 **3 Analytical expressions in the 1-D case**

226 **3.1 Backus homogenization**

227 A vertically transverse isotropic (VTI) medium is an elastic medium with hexag-
 228 onal symmetry and vertical symmetry axis. It can be described by five elastic param-
 229 eters A , C , F , L , and N , also known as the Love parameters (Love, 1906). Supposing
 230 that axis 3 is the symmetry axis, the local \mathbf{S} for a VTI solid can be expressed in Mandel

231 notation as:

$$232 \quad \mathbf{S} = \begin{pmatrix} A & A - 2N & F & 0 & 0 & 0 \\ A - 2N & A & F & 0 & 0 & 0 \\ F & F & C & 0 & 0 & 0 \\ 0 & 0 & 0 & 2L & 0 & 0 \\ 0 & 0 & 0 & 0 & 2L & 0 \\ 0 & 0 & 0 & 0 & 0 & 2N \end{pmatrix}, \quad (5)$$

233 and the level of shear wave radial anisotropy can be written as:

$$234 \quad \xi = \frac{N}{L}. \quad (6)$$

235 Backus (1962) explicitly showed analytical upscaling relations for seismic waves propa-
 236 gating in a 1-D stratified medium. For a 1-D layered medium where each layer is a VTI
 237 medium, the long-wavelength effective medium is also a VTI medium. The effective
 238 equivalent of the elastic constants, for instance, N and L concerning the shear wave
 239 velocities are given by an arithmetic mean and a harmonic mean, respectively:

$$240 \quad N^* = \langle N \rangle, \quad (7)$$

$$241 \quad L^* = \langle 1/L \rangle^{-1}, \quad (8)$$

242 where $\langle \cdot \rangle$ refers to the spatial average over a wavelength of any periodic function (in
 243 this case, N and $1/L$), and $*$ denotes a long wavelength effective property. The effective
 244 density ρ^* is simply the arithmetic mean of the local density ρ :

$$245 \quad \rho^* = \langle \rho \rangle. \quad (9)$$

246 The effective shear wave radial anisotropy ξ^* is essentially the ratio between the effec-
 247 tive equivalents of N and L :

$$248 \quad \xi^* = \frac{N^*}{L^*} = \langle N \rangle \langle 1/L \rangle. \quad (10)$$

249 In this way, for a 1-D fine-scale medium where each layer is isotropic ($N = L$),
 250 the long-wavelength effective medium is transversely isotropic, and the level of extrinsic
 251 radial anisotropy is given by $\langle N \rangle \langle 1/N \rangle$ (Alder et al., 2017).
 252

253 **3.2 An analytical expression to quantify CPO and SPO in a 1-D lay-** 254 **ered media**

255 Let us consider an intrinsically anisotropic (CPO component) and finely-layered
 256 (SPO component) VTI medium. Similar as to how we defined our reference medium

257 in section 2, we regard the elastic parameters N and L as the sum of an isotropic
 258 component defined by the shear moduli μ , and local anisotropic perturbations N_A and
 259 L_A , respectively:

$$260 \quad N(z) = \mu(z) + N_A(z), \quad (11)$$

$$261 \quad L(z) = \mu(z) + L_A(z). \quad (12)$$

262
 263 The isotropic equivalent of μ can be computed as (J.-P. Montagner, 2007; Maupin et
 264 al., 2007):

$$265 \quad \mu = \frac{1}{15}(C + A - 2F + 6L + 5N), \quad (13)$$

266 where A and C are elastic parameters concerning P -waves, and F relates to the
 267 so-called 'ellipticity' (*i.e.*, the velocity along the direction interposing fast and slow
 268 velocities). Assuming no P -wave anisotropy and setting F to unity, one can simplify
 269 equation (13) to:

$$270 \quad \mu = \frac{1}{3}(2L + N). \quad (14)$$

271 Knowing equations (6) and (14), one can re-write N and L in terms of μ and $\xi_{\text{CPO}} =$
 272 N/L giving:

$$273 \quad N = \xi_{\text{CPO}} \frac{3\mu}{2 + \xi_{\text{CPO}}}, \quad (15)$$

$$274 \quad L = \frac{3\mu}{2 + \xi_{\text{CPO}}}. \quad (16)$$

275
 276 It is now straightforward to determine the anisotropic components N_A and L_A by
 277 equating equations (11) and (15). For the sole purpose of segregating the isotropic
 278 and anisotropic components, the forms of N and L consistent with equation (1) is
 279 therefore:

$$280 \quad N(z) = \mu(z) + \left(\xi_{\text{CPO}}(z) \frac{3\mu(z)}{2 + \xi_{\text{CPO}}(z)} - \mu(z) \right), \quad (17)$$

$$281 \quad L(z) = \mu(z) + \left(\frac{3\mu(z)}{2 + \xi_{\text{CPO}}(z)} - \mu(z) \right), \quad (18)$$

282
 283 where any variable as a function of z implies variations in space.

284 To calculate the long-wavelength effective equivalent of such a medium, let us
 285 first write the parameters μ and ξ_{CPO} as:

$$286 \quad \mu(z) = \langle \mu \rangle + \delta\mu(z), \quad (19)$$

$$287 \quad \xi_{\text{CPO}}(z) = \langle \xi_{\text{CPO}} \rangle + \delta\xi_{\text{CPO}}(z), \quad (20)$$

288

289 where $\langle \mu \rangle$ and $\langle \xi_{\text{CPO}} \rangle$ are the spatially-averaged counterparts. $\delta\mu$ and $\delta\xi_{\text{CPO}}$ are small-
 290 scale heterogeneities in the shear modulus and intrinsic radial anisotropy, respectively.
 291 They verify $\langle \delta\mu \rangle$ and $\langle \delta\xi_{\text{CPO}} \rangle = 0$. The long-wavelength effective equivalents N^* and
 292 $1/L^*$ are:

$$293 \quad N^* = \langle N \rangle = \left\langle \xi_{\text{CPO}} \frac{3\mu}{2 + \xi_{\text{CPO}}} \right\rangle = \left\langle (\langle \xi_{\text{CPO}} \rangle + \delta\xi_{\text{CPO}}) \frac{3(\langle \mu \rangle + \delta\mu)}{2 + \langle \xi_{\text{CPO}} \rangle + \delta\xi_{\text{CPO}}} \right\rangle, \quad (21)$$

$$294 \quad 1/L^* = \langle 1/L \rangle = \left\langle \frac{2 + \xi_{\text{CPO}}}{3\mu} \right\rangle = \left\langle \frac{2 + \langle \xi_{\text{CPO}} \rangle + \delta\xi_{\text{CPO}}}{3(\langle \mu \rangle + \delta\mu)} \right\rangle. \quad (22)$$

296 We can simplify equations (21) and (22) by assuming a weak contrast in the shear
 297 modulus $\delta\mu \ll \langle \mu \rangle$. Using a second-order Taylor expansion, we get:

$$298 \quad N^* \approx \frac{3\langle \mu \rangle}{2 + \langle \xi_{\text{CPO}} \rangle} \left(\langle \xi_{\text{CPO}} \rangle - \frac{2}{(2 + \langle \xi_{\text{CPO}} \rangle)^2} \langle \delta\xi_{\text{CPO}}^2 \rangle + \frac{2}{\langle \mu \rangle (2 + \langle \xi_{\text{CPO}} \rangle)} \langle \delta\mu \cdot \delta\xi_{\text{CPO}} \rangle \right), \quad (23)$$

$$299 \quad 1/L^* \approx \frac{2 + \langle \xi_{\text{CPO}} \rangle}{3\langle \mu \rangle} \left(1 + \frac{1}{\langle \mu \rangle^2} \langle \delta\mu^2 \rangle - \frac{1}{\langle \mu \rangle (2 + \langle \xi_{\text{CPO}} \rangle)} \langle \delta\mu \cdot \delta\xi_{\text{CPO}} \rangle \right). \quad (24)$$

301 Using equation (10), we multiply equations (23) and (24) and neglect terms
 302 higher than order two to obtain the full effective radial anisotropy ξ^* due to both
 303 fine-layering and intrinsic anisotropy:

$$304 \quad \xi^* \approx \langle \xi_{\text{CPO}} \rangle - \frac{2}{(2 + \langle \xi_{\text{CPO}} \rangle)^2} \langle \delta\xi_{\text{CPO}}^2 \rangle + \frac{\langle \xi_{\text{CPO}} \rangle}{\langle \mu \rangle^2} \langle \delta\mu^2 \rangle + \frac{2 - \langle \xi_{\text{CPO}} \rangle}{\langle \mu \rangle (2 + \langle \xi_{\text{CPO}} \rangle)} \langle \delta\mu \cdot \delta\xi_{\text{CPO}} \rangle. \quad (25)$$

305 Equation (25) explicitly shows the separate effects of the small-scales in the
 306 isotropic component and in the intrinsically anisotropic component onto the effective
 307 anisotropy as 'seen' by long-period seismic waves. Assuming the medium to be de-
 308 void of intrinsic anisotropy (*i.e.*, $\xi_{\text{CPO}} = 1$ and $\delta\xi_{\text{CPO}} = 0$), the full effective radial
 309 anisotropy ξ^* directly relates to the level of heterogeneities in the shear moduli. Here,
 310 $\langle \delta\mu^2 \rangle$ refers to the variance of small-scale heterogeneities of the shear modulus $\delta\mu$.
 311 It can be interpreted as the extrinsic radial anisotropy ξ_{SPO}^* due to the seismically
 312 unresolved small-scale isotropic heterogeneities. It varies as the square of the hetero-
 313 geneities, in agreement with the result of Alder et al. (2017).

314 On the other hand, when the isotropic component is uniform (*i.e.*, $\delta\mu = 0$), ξ^*
 315 also varies with the square of heterogeneities, but now in intrinsic anisotropy. This
 316 can be interpreted as the effective intrinsic radial anisotropy ξ_{CPO}^* , *i.e.* the intrinsic
 317 anisotropy that gets smoothed out as a result of upscaling. Interestingly, its overall
 318 effect is to reduce the level of intrinsic anisotropy as indicated by the minus δ sign in

319 front of the second term. In the absence of small-scale isotropic heterogeneities, we
 320 anticipate anisotropy to be always underestimated by tomography.

321 Finally, equation (25) suggests the existence of a cross-term $\langle \delta\mu \cdot \delta\xi_{\text{CPO}} \rangle$ due to the
 322 spatial correlation between intrinsic anisotropy and shear modulus. Supposing spatial
 323 variations in both components are significant such as at major seismic discontinuities,
 324 the correlation term should influence the anisotropy mapped in tomographic models.
 325 Nevertheless, it is propounded that this correlation term is usually negligible and hence
 326 may need not be accounted for (Bakulin, 2003).

327 Similarly, the effective Voigt-averaged shear modulus μ^* is given by:

$$328 \quad \mu^* = \frac{2L^* + N^*}{3}. \quad (26)$$

329 Plugging equations (23) and (24) into equation (26), we get:

$$330 \quad \mu^* = \langle \mu \rangle - \frac{2}{\langle \mu \rangle (2 + \langle \xi_{\text{CPO}} \rangle)} \langle \delta\mu^2 \rangle - \frac{2\langle \mu \rangle}{(2 + \langle \xi_{\text{CPO}} \rangle)^3} \langle \delta\xi_{\text{CPO}}^2 \rangle + \frac{4}{(2 + \langle \xi_{\text{CPO}} \rangle)^2} \langle \delta\mu \cdot \delta\xi_{\text{CPO}} \rangle. \quad (27)$$

331 Ignoring intrinsic anisotropy (*i.e.*, $\xi_{\text{CPO}} = 1$ and $\delta\xi_{\text{CPO}} = 0$), the effective shear
 332 modulus μ^* is always smaller than its spatially-averaged version $\langle \mu \rangle$. Such a result
 333 is logical in the 1-D case. Here, radial anisotropy induced by fine-layering is always
 334 positive (equation (25)) thereby having $N^* > L^*$. Since L 'counts' twice and N once
 335 in its isotropic average, its long-wavelength effective equivalent μ^* is always slower
 336 than $\langle \mu \rangle$. Contrastingly, if one neglects isotropic heterogeneities and only consider
 337 variations in intrinsic anisotropy, homogenization also results in the underestimation
 338 of the shear modulus. One would predict that homogenization leads to the creation
 339 of apparent isotropic heterogeneities due to small-scale variations in CPO. Lastly and
 340 as expected, the cross term recurs due to the spatial correlation between the shear
 341 modulus and intrinsic anisotropy.

342 We acknowledge that the homogenized expressions given by equations (25) and
 343 (27) in terms of the isotropic shear modulus μ may not be particularly convenient for
 344 seismologists. In practice, we observe spatial distributions in V_S and not in μ . If one
 345 assumes that density is uniform, then $\delta\mu/\mu$ can be simply replaced by $2\delta V_S/V_S$. On
 346 the other hand, if one assumes that density increases with V_S , one could also establish
 347 long-wavelength effective expressions for V_S in the same manner as μ using simple
 348 empirical relations for density such as that of Tkalčić et al. (2006).

349 In the Earth’s asthenosphere, we do not expect velocity variations (*i.e.* $\Delta V_S/(V_{S1} +$
 350 $V_{S2})$) oftentimes to be larger than 5% (e.g. Xu et al., 2008; Stixrude & Jeanloz, 2015).
 351 This roughly translates to $\sim 10\%$ heterogeneities in the shear modulus assuming con-
 352 stant density ρ . To perform a numerical estimate, let us examine a stack of planar
 353 layers with alternating shear moduli values determined by $\pm \Delta\mu/2$ (Figure 2a middle
 354 panel) corresponding to shear wave velocity variations $\Delta V_S/(V_{S1} + V_{S2})$ of about 10%.
 355 The 1-D depth profiles depict periodic variations with layers of equal thicknesses of
 356 20 km. Positive intrinsic radial anisotropy ($\xi = 1.2$) is prescribed in the even layers,
 357 whereas the odd layers are isotropic ($\xi = 1$) (Figure 2a right panel). After upscaling
 358 over a wavelength much larger than 20 km, the resulting profiles for N^* and L^* are
 359 homogeneous, and simply given by their arithmetic and harmonic means, respectively
 360 (Figure 2a left panel). Once the long-wavelength effective N^* and L^* are acquired, we
 361 can compute the full effective radial anisotropy ξ^* through equation (10) (solid red line
 362 in Figure 2a right panel), and the effective shear modulus μ^* through equation (26)
 363 (solid red line in Figure 2a middle panel). Figure 2b illustrates a different scenario
 364 where ξ only exists in the odd layers (Figure 2b right panel). In essence when the
 365 shear modulus and intrinsic anisotropy are uncorrelated, the homogenized parameters
 366 μ^* and ξ^* should be the same regardless. However, a slight offset in μ^* and ξ^* of
 367 Figure 2b with respect to Figure 2a can be observed which is exclusively attributed to
 368 this cross term as hinted by equations (25) and (27). Strictly speaking, the reduction
 369 in the amplitude of the effective properties arises from the switch in signs in the cross
 370 term from positive to negative $\langle \delta\mu \cdot \delta\xi \rangle$, implying that in the second scenario, the shear
 371 modulus and intrinsic anisotropy are now anti-correlated.

372 To validate the second-order approximation, we also show ξ^* and μ^* using equa-
 373 tions (25) and (27) respectively (dashed blue lines in Figures 2a and 2b middle and
 374 right panels). Clearly by applying equation (25), the intrinsic component (first term)
 375 contributes the most to the effective anisotropy with $1 - \langle \xi_{CPO} \rangle = 0.1$ wherein its spa-
 376 tial variations’ overall effect is to tone-down the amplitude of anisotropy by an amount
 377 of $\sim -10^{-3}$ (second term). This is followed by the SPO component (third term) which
 378 is responsible for the amplification of anisotropy ($\sim +10^{-2}$). Lastly, the cross term
 379 provides the least contribution ($\sim \pm 10^{-3}$) and therefore can reasonably be ignored in
 380 most cases. The \pm sign denotes that it may increase or decrease anisotropy depending
 381 on the coupling pattern between the shear modulus and intrinsic anisotropy.

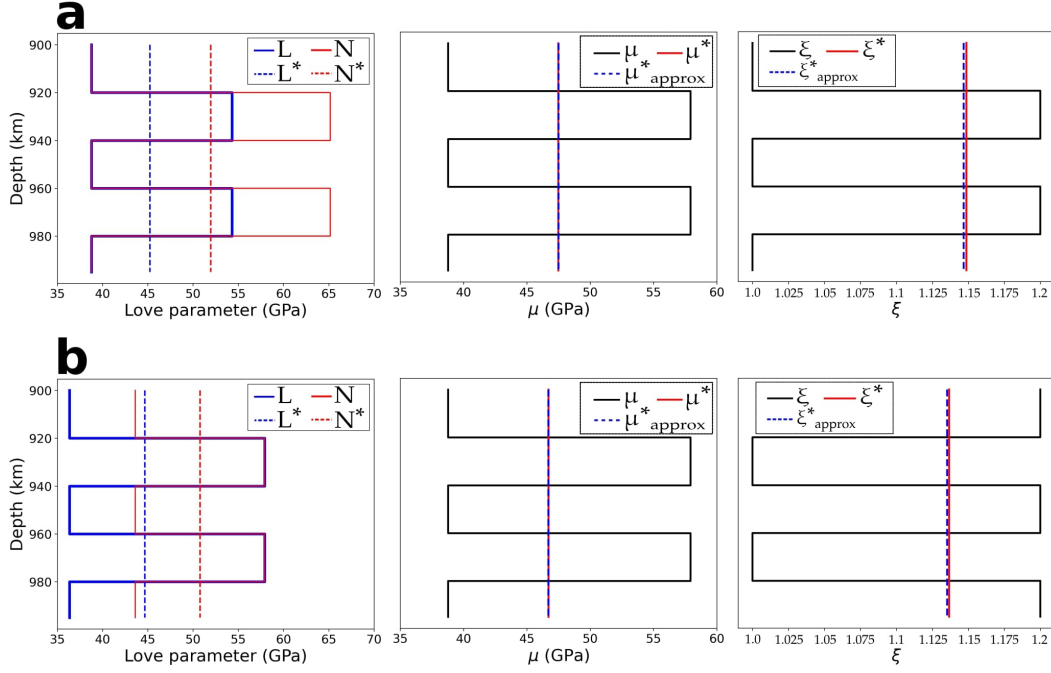


Figure 2. 1-D binary and periodic media with 10% isotropic heterogeneities in terms of $\Delta V_S/(V_{S1} + V_{S2})$ prescribed across: (a) even layers, and (b) odd layers. Upon homogenization, the resulting profiles are homogeneous (variables denoted by (*)). The dashed blue lines at the middle (μ_{approx}^*) and right panels (ξ_{approx}^*) correspond to the predicted long-wavelength effective equivalents using the second order approximations from equations (27) and (25), respectively. The difference in the homogenized shear moduli and radial anisotropy between (a) and (b) is attributed to the cross term as implied by equation (25). Since the medium is periodic, it is enough to only display a portion of the medium.

3.3 Composite law for radial anisotropy

In this section, we show how the total effective anisotropy can be expressed in terms of its intrinsic and extrinsic contributions. For that, we investigate two special cases: (1) a purely isotropic 1-D layered medium, (2) a purely anisotropic 1-D medium (*i.e.*, no spatial variations in isotropic component), and find equivalent expressions for extrinsic radial anisotropy ξ_{SPO}^* and effective intrinsic radial anisotropy ξ_{CPO}^* . By doing so, we elicit a simple composite law related to equation (25) that can be extrapolated to 2-D and 3-D media.

In the case of an isotropic medium with spatially-varying shear modulus, the radial anisotropy is entirely due to SPO. Equation (25) reforms into:

$$\xi_{\text{SPO}}^* \approx 1 + \frac{1}{\langle \mu \rangle^2} \langle \delta \mu^2 \rangle. \quad (28)$$

On the other hand, a purely anisotropic medium without spatial variations in the shear modulus leads to an effective intrinsic anisotropy:

$$\xi_{\text{CPO}}^* \approx \langle \xi_{\text{CPO}} \rangle - \frac{2}{(2 + \langle \xi_{\text{CPO}} \rangle)^2} \langle \delta \xi_{\text{CPO}}^2 \rangle. \quad (29)$$

By taking the product between equations (28) and (29), neglecting terms higher than order two, one has simply:

$$\xi_{\text{CPO}}^* \times \xi_{\text{SPO}}^* \approx \langle \xi_{\text{CPO}} \rangle - \frac{2}{(2 + \langle \xi_{\text{CPO}} \rangle)^2} \langle \delta \xi_{\text{CPO}}^2 \rangle + \frac{\langle \xi_{\text{CPO}} \rangle}{\langle \mu \rangle^2} \langle \delta \mu^2 \rangle, \quad (30)$$

which is approximately equal to ξ^* in equation (25) but without the cross term. Therefore, ignoring spatial correlations between intrinsic anisotropy and shear modulus, the full effective radial anisotropy can be quantified through the following composite law:

$$\xi^* \approx \xi_{\text{CPO}}^* \times \xi_{\text{SPO}}^*. \quad (31)$$

In practice, ξ^* can be estimated from a tomographic inversion (Debayle & Kennett, 2000; Plomerová et al., 2002; Gung et al., 2003; Nettles & Dziewoński, 2008a; Fichtner et al., 2010). Seismologists often compare ξ^* with the intrinsic radial anisotropy ξ_{CPO} computed from a geodynamically-based CPO model (Becker et al., 2003, 2006; Ferreira et al., 2019; Sturgeon et al., 2019). The comparison should be done instead with an effective model ξ_{CPO}^* , which is difficult to estimate without access to any elastic homogenization tools. Furthermore, equation (25) suggests that there is a non-negligible extrinsic component of anisotropy due to the unresolved small-scale isotropic

411 heterogeneities. While it is difficult to rigorously establish analytical solutions in the
 412 case of a 2-D/3-D complex media, following the logic above, we hypothesize that the
 413 mismatch often observed between homogenized CPO models and tomographic models
 414 is the extrinsic radial anisotropy ξ_{SPO}^* .

415 **4 Methods for 2-D media**

416 **4.1 Homogenization in 2-D and in 3-D media**

417 The classic homogenization method of Backus is only applicable in 1-D to media
 418 exhibiting spatial periodicity. The true Earth, however, is a complex 3-D and multi-
 419 scale medium. To alleviate this problem and quantify effective elastic properties in
 420 a mantle-like medium, we rely on the non-periodic elastic homogenization technique
 421 developed by Capdeville and Marigo (2007); Capdeville et al. (2010); Guillot et al.
 422 (2010); Capdeville et al. (2015). Originally, this method has been developed as a pre-
 423 processing step enabling one to solve the elastostatic wave equation using a simple
 424 mesh, speeding up the computations for wave propagation in complex media. It has
 425 also been used to improve the convergence and computational cost of full waveform
 426 inversion (Capdeville & Métivier, 2018; Hedjazian et al., 2021).

427 In the non-periodic case, the homogenization is not performed with respect to the
 428 periodicity of the medium, but with respect to the minimum wavelength present in the
 429 wavefield. The assumption that this minimum wavelength λ_{min} exists is required for
 430 non-periodic medium with no scale separation such as the true Earth. Scales smaller
 431 than λ_{min} are seen by the wavefield only through their effective properties. To sep-
 432 arate the small and the large scales, we need to define a threshold wavelength λ_h ,
 433 called the homogenization wavelength. λ_h is a user-defined parameter, and all scales
 434 smaller than λ_h are homogenized. Numerical examples suggest that, for all natural
 435 media, homogenization with a value $\lambda_h = 0.5\lambda_{\text{min}}$ is sufficient to accurately reproduce
 436 the complete wavefield (Capdeville et al., 2010). Hence, this value is chosen in the
 437 rest of the present study. Computing the effective properties of an elastic medium
 438 with homogenization wavelength λ_h requires to solve an elastostatic problem numer-
 439 ically. To do this, we use the 3-D Fast-Fourier Homogenization algorithm developed
 440 by Capdeville et al. (2015).

Assuming a good data coverage, Capdeville and Métivier (2018) numerically verified that for complex elastic media, a seismic tomography model and the homogenized model are in agreement at spatial wavelengths higher than λ_h . Hence, homogenization can be viewed as a first-order tomographic operator. We will consider the homogenized model as the best image one could get from seismic tomography. This can be translated to:

$$\mathbf{S}^* = \mathcal{H}(\mathbf{S}) \quad (32)$$

where \mathcal{H} is the tomographic operator, \mathbf{S} is the reference medium, and the homogenized model \mathbf{S}^* is the full effective medium (*i.e.*, the best recovered image as seen by a wavefield of a given minimum wavelength λ_{\min} and assuming perfect data coverage). In this paper, we apply this 'tomographic operator' to a 2-D composite medium by upscaling the marble cake model in the presence of deformation-induced anisotropy.

4.2 Isotropic heterogeneities in a 2-D mechanically-mixed mantle

To define our 2-D incompressible flow model imitating mantle convection, we use a stream function similar to that of Alder et al. (2017):

$$\Psi(x, z, t) = \sin(a\pi z) \left[\sin(b\pi x) + \alpha(t) \sin((b+1)\pi x) + \beta(t) \sin((b+2)\pi x) \right] \quad (33)$$

where $\alpha(t)$ and $\beta(t)$ are sinusoidal functions of time that introduces chaotic mixing. The variables a and b relate to the number of distinguishable convection cells and are chosen arbitrarily. The form of the function Ψ ensures free-slip boundary conditions. Finally, the resulting velocity field is scaled using a reference value of $1 \text{ cm}\cdot\text{yr}^{-1}$.

We replicate the marble cake patterns by deforming a circular anomaly at the center of the box using our prescribed flow field. To do this, control points that define the contour of the anomaly are advected using fourth-order Runge Kutta methods with variable time-stepping (Press et al., 1992). To achieve a final configuration for the anomaly, we define an advection mixing time T_{SPO} . Figure 3 illustrates the evolution of the pattern when subjected to the flow field defined in equation (33). Setting $a = 1$, $b = 2$, and $T_{\text{SPO}} = 75 \text{ My}$, we have a mechanically-mixed medium with two characteristic convection cells.

Using the last panel of Figure 3, the binary system is defined by assigning a reference S-wave velocity value $V_{S_2} = 4.52 \text{ km}\cdot\text{s}^{-1}$ to the yellow region, and $V_{S_1} =$

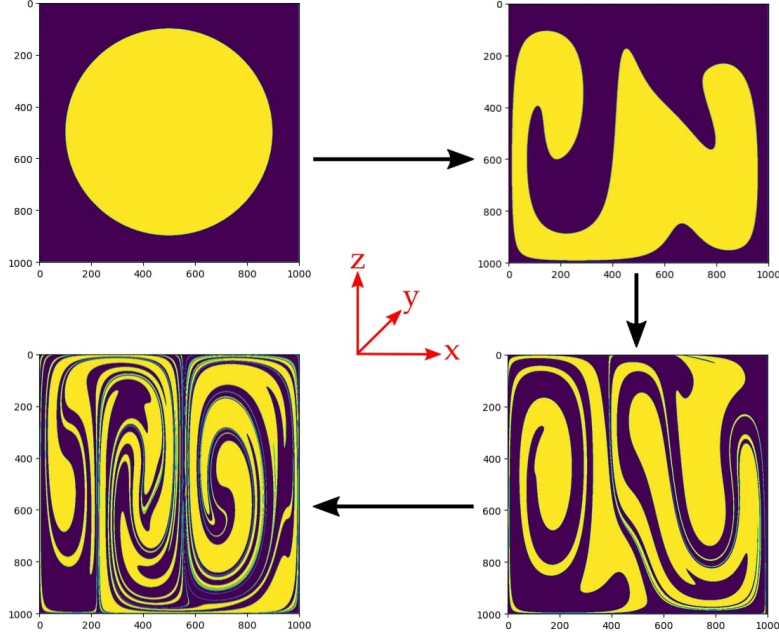


Figure 3. Initially a circle, the anomaly is deformed progressively until the medium reaches a stage resembling marble cake-like patterns.

471 $3.7 \text{ km}\cdot\text{s}^{-1}$ to the purple region so that the level of isotropic heterogeneities is given
 472 by $100\% \times (V_{S_1} - V_{S_2}) / (V_{S_1} + V_{S_2}) = 10\%$. P -wave velocities are computed by
 473 imposing a constant ratio $V_P/V_S = 1.7$ (Obrebski et al., 2010). Following the work
 474 of Tkalčić et al. (2006), we compute the density ρ using the empirical relation $\rho =$
 475 $2.35 + 0.036(V_P - 3)^2$. These values are used to define the local isotropic tensor \mathbf{S}_I in
 476 equation (1).

477 4.3 Modeling of Crystallographic Preferred Orientation

478 Crystallographic preferred orientation of mantle minerals forms due to strain
 479 accumulation over time. The velocity gradient tensor field of the marble cake model
 480 $\nabla \mathbf{u}$ is derived from the stream function Ψ described previously. We then model CPO
 481 evolution of olivine aggregates using D-Rex, a program which calculates strain-induced
 482 CPO by plastic deformation, and dynamic recrystallization (E. Kaminski et al., 2004).
 483 The activities of olivine slip systems are chosen to correspond to dry mantle conditions,
 484 while other parameters are taken as in the reference D-Rex model. A time scale for
 485 CPO evolution T_{CPO} is defined to control the level of intrinsic anisotropy.

486 In our numerical experiments, we compute CPO everywhere irrespective of the
 487 actual mineralogical phase. We scale the elastic tensor derived from D-Rex so that
 488 its isotropic component is identical to the binary system derived in Section 4.2. The
 489 reference medium can be constructed from equation (1) where \mathbf{S}_I now relates to the
 490 small-scale isotropic heterogeneities in the mechanically-mixed mantle, and \mathbf{S}_A is the
 491 intrinsically anisotropic component computed with D-Rex.

492 4.4 Quantifying the level of anisotropy

493 In this section, we define two ways to quantify the level of seismic anisotropy
 494 for any given elastic tensor \mathbf{S} . The first one is radial anisotropy. We project the
 495 elastic tensor in terms of an azimuthally-averaged vertically transverse isotropic (VTI)
 496 medium to obtain a tensor described as in equation (5). Here, the parameters L and
 497 N can be computed from \mathbf{S} as follows (J.-P. Montagner & Nataf, 1986):

$$498 \quad L = \frac{1}{2}(S_{44} + S_{55}) \quad (34)$$

$$499 \quad N = \frac{1}{8}(S_{11} + S_{22}) - \frac{1}{4}S_{12} + \frac{1}{2}S_{66}. \quad (35)$$

501 The level of radial anisotropy is then given by equation (6).

502 Another convenient way to quantify anisotropy is to compute the percentage of
 503 total anisotropy by taking the L2-norm fraction of the anisotropic part of the elastic
 504 tensor with respect to the isotropic part. This quantity is called the anisotropy index
 505 and is given by:

$$506 \quad \text{anisotropy index} = \frac{\|\mathbf{S} - \mathbf{S}_I\|}{\|\mathbf{S}_I\|}. \quad (36)$$

507 5 Elastic homogenization of a 2-D mechanically-mixed mantle in the 508 presence of CPO

509 Figure 4 displays some seismic properties of the reference medium \mathbf{S} before and
 510 after homogenization. The left panels are the true structures, whereas the middle and
 511 right panels are the structures equating to the full effective medium $\mathcal{H}(\mathbf{S})$ at homog-
 512 enization wavelengths λ_h of 200 km and 500 km, respectively. The first row depicts
 513 the shear wave velocities. The anisotropy characterized by its radial component, and
 514 by its norm fraction are depicted in the second row and in the third row, respectively.
 515 Each pixel initially contains an isotropic part derived from the marble cake model with
 516 a mixing time for advection $T_{\text{SPO}} \sim 75$ My, and an anisotropic part computed from a

517 CPO model with a time scale for CPO evolution of $T_{\text{CPO}} \sim 40$ My corresponding to a
 518 moderately developed crystal fabric. Hereafter, we run our simulation in a box of size
 519 1000×1000 km, define $\lambda_{\text{max}} = 1000$ km as the length scale of our simulations.

520 Several glaring features can be observed such as the presence of positive radial
 521 anisotropy ($\xi > 1$) at the top and bottom boundaries where flow is sub-horizontal,
 522 and likewise negative ($\xi < 1$) at regions where the flow is sub-vertical. As expected,
 523 homogenization results in the smoothing of the structures with the level of smoothing
 524 modulated by λ_h . However, homogenization is not just a simple spatial average but
 525 a product of highly non-linear upscaling relations. With increasing homogenization
 526 wavelengths, the full effective medium becomes devoid of anisotropy in some areas.

527 After decomposing \mathbf{S} into an isotropic tensor $\mathcal{I}(\mathbf{S})$ and an anisotropic tensor $\mathcal{A}(\mathbf{S})$
 528 through equations (2) and (4), one can also homogenize and analyze each component
 529 separately, i.e. $\mathcal{H}(\mathcal{I}(\mathbf{S}))$ and $\mathcal{H}(\mathcal{A}(\mathbf{S}))$. Figure 5 shows the level of effective radial
 530 anisotropy of these two separate components after homogenization. The top panels
 531 recreate the results of Alder et al. (2017). Indeed, homogenizing the fine-layered
 532 isotropic medium produces extrinsic radial anisotropy ξ_{SPO}^* (i.e., radial anisotropy of
 533 model $\mathcal{H}(\mathcal{I}(\mathbf{S}))$). Notice that the patterns of effective intrinsic radial anisotropy and
 534 extrinsic radial anisotropy maps are roughly similar. For example, they both induce a
 535 positive radial anisotropy $\xi > 1$ in the horizontal layers: the stretched heterogeneities
 536 that induce SPO become elongated along the direction of the maximum principal strain
 537 rate that also controls the CPO.

538 Figure 6 depicts the apparent isotropic heterogeneities created upon homoge-
 539 nization of $\mathcal{A}(\mathbf{S})$. It produces maximum velocity perturbations of about 0.25 % at
 540 $\lambda_h = 200$ km and 0.2 % at $\lambda_h = 500$ km. It appears to be a small effect, especially
 541 considering the large and sharp variations of intrinsic anisotropy in our CPO model.

542 To better illustrate the behaviour of different contributions to anisotropy, we
 543 plot in Figure 7 the amplitude of radial anisotropy (in terms of its standard deviation
 544 over the entire 2-D model domain) against the wavelength of homogenization λ_h . In
 545 the following cases, the intrinsic anisotropy component of the reference medium \mathbf{S} is
 546 computed for a CPO developing over increasing duration T_{CPO} of 5, 40, or 75 Myr.
 547 Several points can be noted in Figure 7:

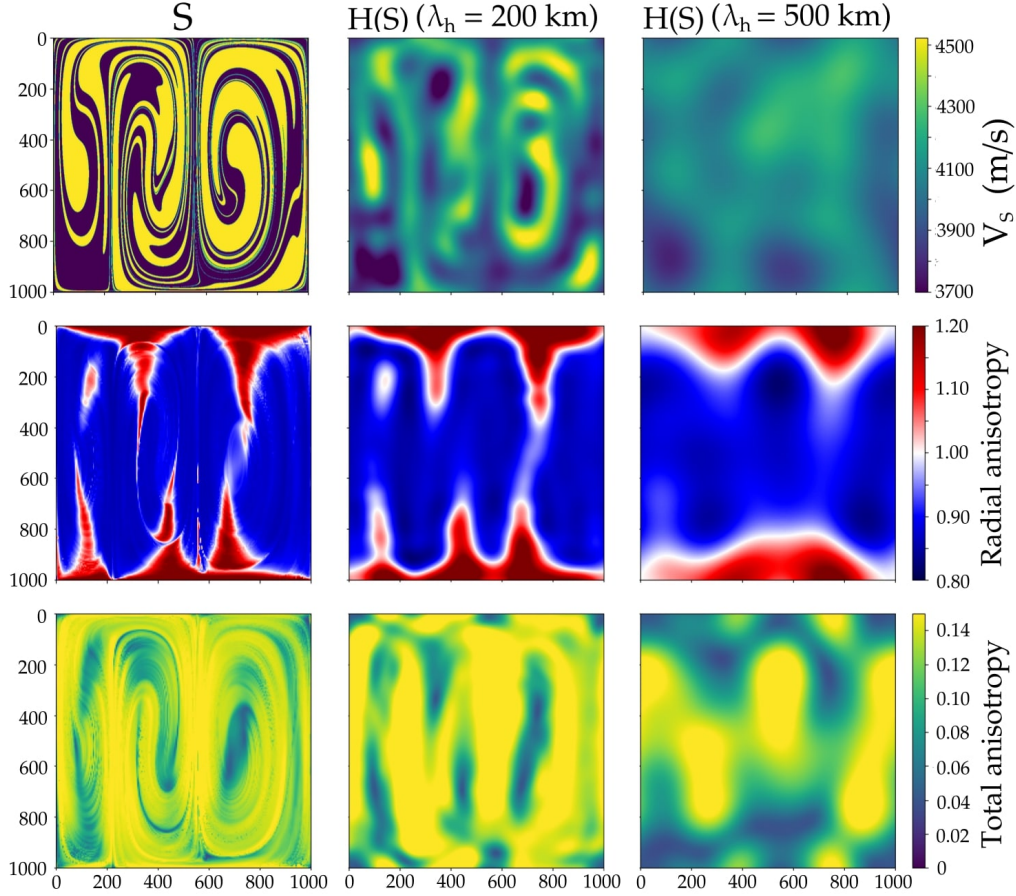


Figure 4. Seismic properties of the reference medium \mathbf{S} before and after homogenization. The model dimensions are $1000 \text{ km} \times 1000 \text{ km} \times 1000 \text{ km}$, with cell sizes of $5 \text{ km} \times 5 \text{ km} \times 5 \text{ km}$. Here, each pixel contains an \mathbf{S} which consists of small-scale isotropic heterogeneities and an intrinsically anisotropic perturbation computed with D-Rex (E. Kaminski et al., 2004). The present-day marble cake patterns correspond to a mixing time for advection $T_{\text{SPO}} \sim 75 \text{ My}$, whereas the time scale for CPO evolution is $T_{\text{CPO}} \sim 40 \text{ My}$. We homogenized \mathbf{S} using the Fast-Fourier homogenization algorithm of Capdeville et al. (2015). (From left to right) First row: V_s models derived from \mathbf{S} , $\mathcal{H}(\mathbf{S})$ at $\lambda_h = 200 \text{ km}$, and $\mathcal{H}(\mathbf{S})$ at $\lambda_h = 500 \text{ km}$. Second row: ξ_{CPO} , ξ^* at $\lambda_h = 200 \text{ km}$, and ξ^* at $\lambda_h = 500 \text{ km}$. Last row: Total anisotropy in terms of the norm fraction of \mathbf{S} , $\mathcal{H}(\mathbf{S})$ at $\lambda_h = 200 \text{ km}$, and $\mathcal{H}(\mathbf{S})$ at $\lambda_h = 500 \text{ km}$. Elastic homogenization can be viewed as the best possible model reconstructed by seismic tomography assuming perfect ray-path coverage.

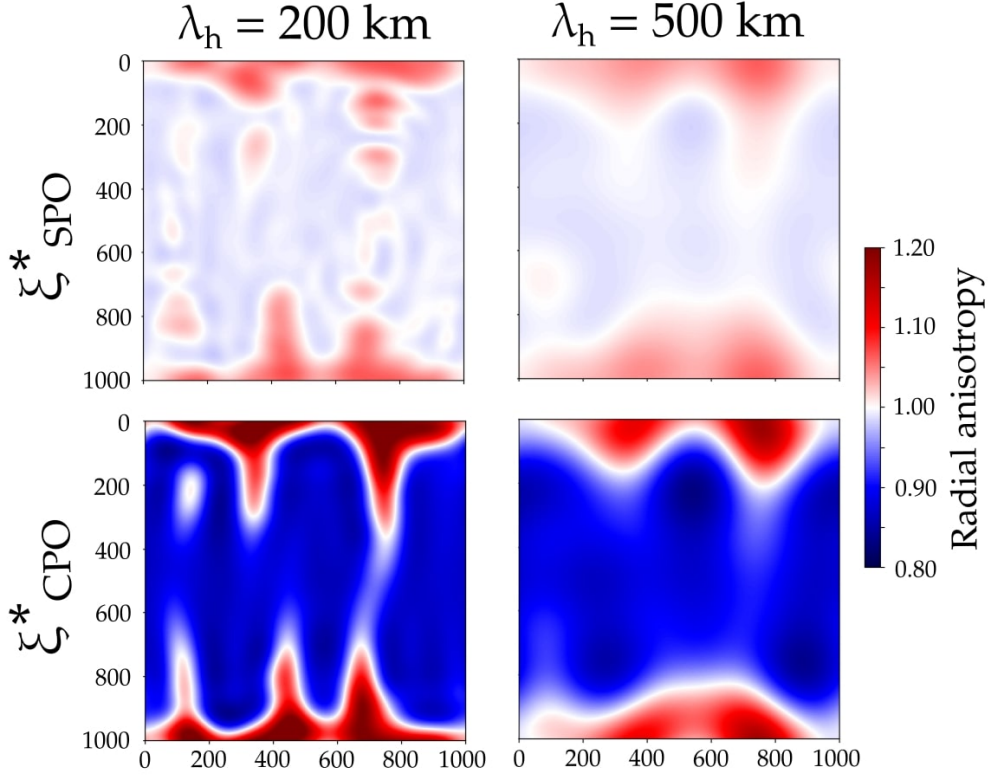


Figure 5. Extrinsic radial anisotropy ξ_{SPO}^* (*i.e.*, radial anisotropy of model $\mathcal{H}(\mathcal{I}(\mathbf{S}))$) (top panels) at two different wavelengths of homogenization λ_h . Here, $\xi_{\text{SPO}}^* > 1$ is now interpreted as horizontal layering whereas < 1 as vertical layering. The bottom panels show the effective intrinsic radial anisotropy ξ_{CPO}^* (*i.e.*, radial anisotropy of model $\mathcal{H}(\mathcal{A}(\mathbf{S}))$).

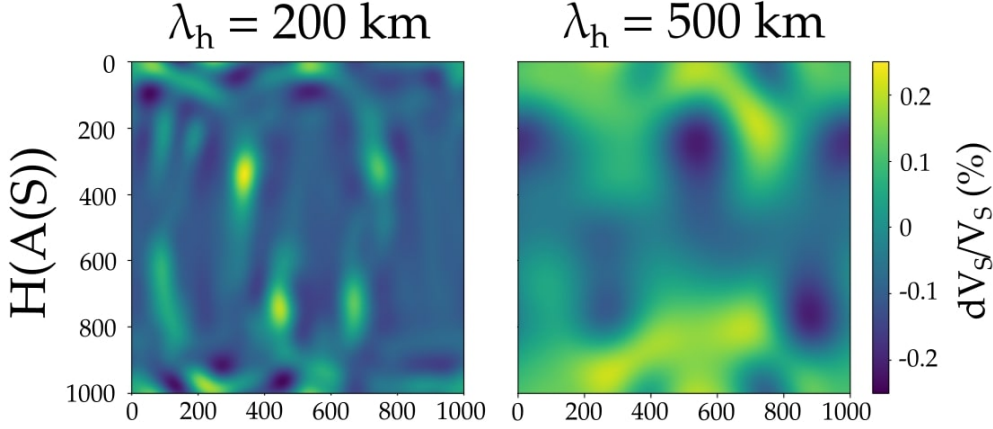


Figure 6. Apparent isotropic velocity perturbations with respect to a mean velocity V_S at two different wavelengths of homogenization λ_h . $\mathcal{H}(\mathcal{A}(\mathbf{S}))$ pertains to the homogenized model of a purely anisotropic medium. Even when placed in a very favorable scenario for intrinsic anisotropy, homogenizing a purely anisotropic medium produces a meager 0.25% artificial heterogeneities at $\lambda_h = 200$ km and 0.2% at $\lambda_h = 500$ km.

548 (i) The resulting intrinsic radial anisotropy ξ_{CPO} in terms of its standard deviation
 549 over the entire region (dashed lines) increases with T_{CPO} , although some saturation
 550 is observed (*i.e.*, the orientation of crystals depends mostly on their recent
 551 deformation, and lose the memory of the deformation they underwent too long ago).

552 (ii) The level of intrinsic anisotropy is diminished upon homogenization. ξ_{CPO}^*
 553 (hollow squares) is always lower than the reference value ξ_{CPO} (dashed lines), and
 554 diminishes with λ_h . This effect can be easily understood. For small λ_h , the wavelength
 555 of homogenization is small compared to the scale of deformation patterns (of order 100
 556 km). At each point of the 2-D map, the direction of CPO is therefore locally constant
 557 over λ_h , which yields $\xi_{\text{CPO}}^* \approx \xi_{\text{CPO}}$. At larger scales, when λ_h increases compared to
 558 the scale of convection, this direction becomes likely random and CPO heterogeneities
 559 averaged over λ_h have different orientations: there is less of a preferential direction
 560 and the averaged level of CPO anisotropy is diminished.

561 (iii) On the contrary, the full effective radial anisotropy ξ^* at short wavelengths
 562 of homogenization λ_h is larger than ξ_{CPO} . This is in agreement with the analytical
 563 expression given by equation (25). This additional anisotropy is of course due to the
 564 existence of SPO (black circles) which reinforces the total level of effective anisotropy.

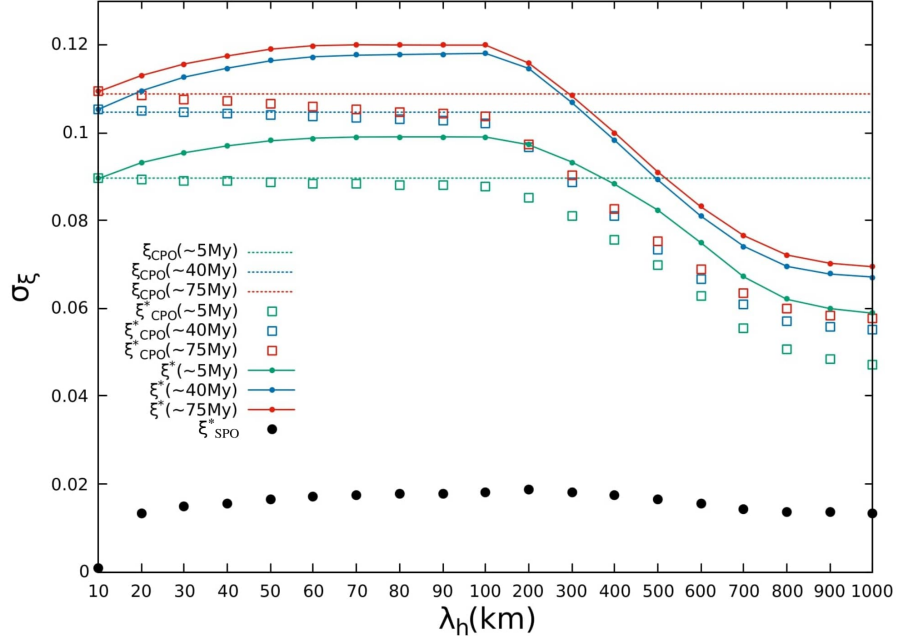


Figure 7. Effective radial anisotropy in terms of its standard deviation σ_ξ over the entire 2-D image, plotted as a function of homogenization length. The time scales indicated in million years pertain to the evolution history of CPO (a larger time scale leads to stronger CPO). Dashed lines represent the standard deviation of ξ_{CPO} in model \mathbf{S} and serve as reference values. In this experiment, ξ_{SPO}^* of model $\mathcal{H}(\mathcal{I}(\mathbf{S}))$ (black circles) deemed to be five times smaller than ξ_{CPO}^* of model $\mathcal{H}(\mathcal{A}(\mathbf{S}))$ (hollow squares). Since SPO is mostly in-phase with CPO, the two anisotropic components add constructively giving the full effective radial anisotropy ξ^* (solid line-dots).

565 (iv) Both ξ_{CPO}^* and ξ^* converge toward ξ_{CPO} at infinitely short homogenization
 566 wavelengths. Only in this unrealistic case (*i.e.*, the perfect recording of the seismic
 567 wavefield up to infinitely short periods), would seismic tomography be able to map the
 568 true intrinsic anisotropy.

569 (v) Extrinsic radial anisotropy ξ_{SPO}^* here has an amplitude that is five times
 570 smaller than ξ_{CPO}^* . Such a result, of course, is specific to this numerical experiment,
 571 and that CPO is indeed stronger than SPO might not be always true. For instance, a
 572 longer mixing time would have resulted in a thinner and more complex layering that
 573 would have increased the SPO. We are unfortunately limited by the number of tracers
 574 necessary to describe the phase stirring which is exponentially increasing with time.

575 5.1 Verifying the composite law $\xi^* = \xi_{\text{CPO}}^* \times \xi_{\text{SPO}}^*$ in 2-D

576 In this section, we aim to verify numerically equation (31) in 2-D by plotting ξ_{SPO}^*
 577 $\times \xi_{\text{CPO}}^*$ against ξ^* for each pixel in our 2-D maps of radial anisotropy. Here again,
 578 the three quantities ξ_{SPO}^* , ξ_{CPO}^* , and ξ^* are respectively computed from $\mathcal{H}(\mathcal{I}(\mathbf{S}))$,
 579 $\mathcal{H}(\mathcal{A}(\mathbf{S}))$, and $\mathcal{H}(\mathbf{S})$. In this case, there is no spatial correlation between CPO and
 580 isotropic heterogeneities in the marble cake, and the effect of the cross-term should be
 581 mitigated. Figure 8b shows this for two different homogenization wavelengths λ_h . We
 582 can see that the relation holds exceptionally well even for large λ_h .

583 In practice however, tomographic models of ξ^* are interpreted in terms of intrinsic
 584 anisotropy, and directly compared with ξ_{CPO} computed from CPO models (Becker et
 585 al., 2003, 2006; Ferreira et al., 2019). We mimic this scenario by comparing ξ_{SPO}^*
 586 $\times \xi_{\text{CPO}}$ instead with ξ^* (Figure 8a). As it turns out, the relation only holds for
 587 small values of λ_h . At larger values of λ_h , the trend appears to be more dispersed as a
 588 consequence of the averaging process, losing its viability to some extent. In the absence
 589 of a homogenized CPO model, we project that this composite law would remain true
 590 in general under the condition that the minimum wavelength used in tomography is
 591 sufficiently small.

592 To test the effect of the rigidity-anisotropy cross-term, we consider another man-
 593 tle model where CPO is only present in one of the two phases of the 2-D marble cake
 594 illustrated in Figure 3. In addition, we increase the percentage of isotropic hetero-
 595 geneities in V_S to 15%. This increases the correlation between the shear modulus and

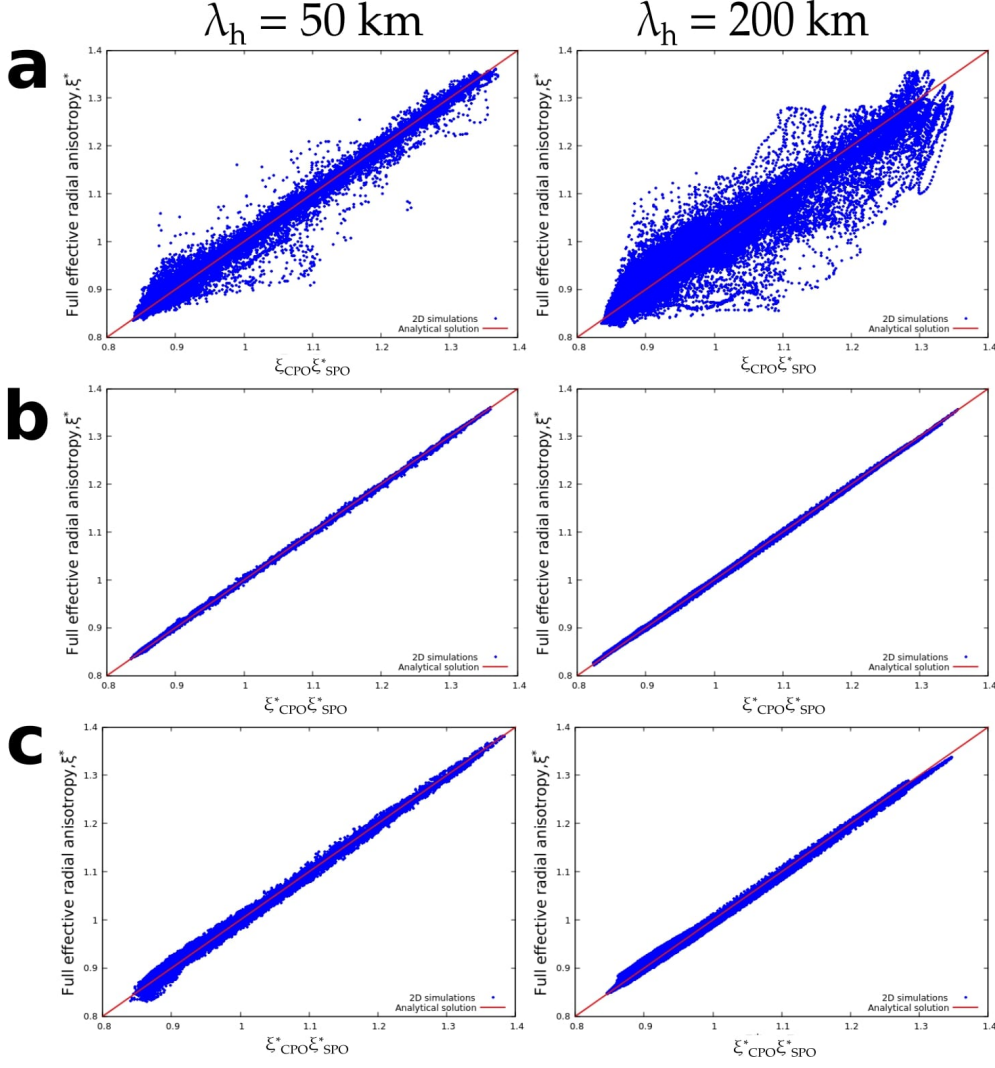


Figure 8. For each pixel i on our 2-D maps of ξ^* , ξ_{CPO} , ξ_{CPO}^* , and ξ_{SPO}^* Figure 8a: , we plot a cloud of points with coordinates: (a) $[\xi_{\text{CPO}} \times \xi_{\text{SPO}}^*(i), \xi^*(i)]$, (b) $[\xi_{\text{CPO}}^* \times \xi_{\text{SPO}}^*(i), \xi^*(i)]$ overlaying the analytical solution equation (31) (solid red lines). Our numerical simulations suggest that CPO models should be homogenized first before comparing with tomographic models. Figure 8c displays the effect of the cross term by increasing isotropic heterogeneities to 15% and by prescribing CPO only in the yellow phases of the marble cake model in Figure 3.

596 intrinsic anisotropy. Figure 8c displays the numerical solution at $\lambda_h = 50$ km and
 597 200 km when CPO is computed in the yellow phases alone. Based on our analytical
 598 results, the points are much more spread-out than that of Figure 8b. In this scenario,
 599 CPO now varies sharply and in the same places as isotropic discontinuities (*i.e.*, $\delta\xi_{\text{CPO}}$
 600 terms in equation (25) are much larger), and as expected the cross-term is much more
 601 apparent. Nonetheless, this only produces small departures from the composite law
 602 (red line), implying that the predictions carried out by the composite law are robust.

603 5.2 Discussion

604 We investigated the effects of elastic homogenization to a specific class of fine-
 605 scale, marble cake-like models of the mantle in the presence of deformation-induced
 606 anisotropy. The homogenization procedure can be viewed as a tomographic operator
 607 applied to a reference elastic model (Capdeville et al., 2013).

608 We showed that the extrinsic radial anisotropy produced by fine-layering could
 609 reach up to 2% (see Figure 7) assuming 10% of isotropic heterogeneities. This anisotropy
 610 is much lower than the one induced by CPO where the effective intrinsic radial
 611 anisotropy could peak at nearly 11%. This result is however modulated by some
 612 parameters that regulate the level of effective anisotropy. For example, the layered fil-
 613 aments contrived from our marble cake models are of the order 10 – 100 km whereas of
 614 those proposed by Allègre and Turcotte (1986) are much thinner and can stretch even
 615 further down to the centimeter scale, which would induce larger extrinsic anisotropy.
 616 Next is more of on the intrinsic aspect. Since CPO results from finite strain accumu-
 617 lation over time, the amplitude of intrinsic anisotropy increases with the time scale for
 618 CPO evolution T_{CPO} . Such presumptions may only be valid in regions where rock de-
 619 formation varies over extended periods of time, although recrystallization and damage
 620 would limit the CPO that can be eventually accumulated (Ricard & Bercovici, 2009).
 621 Furthermore, we considered olivine of type-A crystal fabric as the solitary anisotropic
 622 mineral in our mantle models. Because of this, the intrinsic anisotropy produced from
 623 finite deformation should be seen as an upper bound. Inclusion of other anisotropic
 624 minerals such as pyroxene which make up a fraction in mantle periodotite (Maupin
 625 & Park, 2015) would change the net anisotropy. For instance, we anticipate that in-
 626 cluding a substantial amount of enstatite would dilute the amount of anisotropy (e.g.
 627 E. Kaminski et al., 2004). Therefore, whether CPO accounts for most of the bulk

628 anisotropy observed in tomographic images remains inconclusive and needs further
629 verification.

630 In light of the simulations conducted, we expect large-scale anisotropy to be
631 only overestimated when CPO coexists with significant SPO as exemplified in our
632 simulations. In the absence of SPO, homogenization can only decrease the strength of
633 anisotropy. By accounting for both contributions, we showed that $\xi > 1$ is attributed
634 to a combination of lateral flow and horizontal layering, and $\xi < 1$ is a combination
635 of flow ascent and vertical layering. Indeed, the direction of shear not only dictates
636 the preferred orientation of the anisotropic minerals, but also of the orientation of the
637 folded strips that gives rise to fine-layering.

638 The repercussion of homogenizing intrinsic anisotropy alone amounts to the
639 convection-scale averaging of the CPO as evidenced by our simulations. By defini-
640 tion, intrinsic anisotropy develops from the preferred alignment of the minerals at the
641 crystal level. This explains why we can map-out the fast axis of anisotropy at an
642 arbitrary location. When long period observations sample an intrinsically anisotropic
643 medium, the wavefield spatially-averages these orientations. As a result, preferential
644 orientations that are products of imbricated convection tend to appear more het-
645 erogeneous, thereby ostensibly losing intrinsic anisotropy upon homogenization. In
646 contrast, spatially-coherent preferential orientations produced by simpler convection
647 patterns are less susceptible to the dilution of intrinsic anisotropy.

648 The applicability of equation (31) in a 2-D complex media may be of interest
649 to geodynamicists and tomographers alike. Not only does it permit one to directly
650 quantify the discrepancy between the full effective radial anisotropy inferred from
651 a tomographic model and the effective intrinsic radial anisotropy computed from a
652 homogenized CPO model, it further solidifies the supposition that the mismatch is in-
653 deed a result of extrinsic radial anisotropy due to the seismically-unresolved small-scale
654 isotropic heterogeneities. We have conducted several numerical experiments to prove
655 that the composite law still holds exceptionally well even when the rigidity-intrinsic
656 anisotropy cross term is amplified. Erroneous interpretation of a CPO model to explain
657 tomographic observations may therefore be avoided with the help of homogenization.

658 The conclusions reached in this section are based on two assumptions: (1) We
659 held the isotropic velocity contrast at a fixed value and assumed it to be representative

660 of the entire mantle. In reality however, V_S variations between two-end member com-
 661 positions generally decrease with depth (Xu et al., 2008; Stixrude & Jeanloz, 2015).
 662 This is not to mention the local presence of melt and water that contributes to the vari-
 663 ations in wave velocities, and hence the strength of heterogeneities which completely
 664 alters the level of apparent anisotropy. (2) We disregarded the dependency of the elas-
 665 tic constants built from our mantle models on pressure P and temperature T . Future
 666 avenues one could take would be to incorporate $P - T$ dependence using empirical
 667 relations constrained from laboratory experiments. For instance, one may compute
 668 $P - T$ dependence using first-order corrections around a reference elastic tensor at
 669 ambient $P - T$ conditions (Estey & Douglas, 1986). The availability of self-consistent
 670 thermodynamic models based on free-energy minimization schemes (J. A. Connolly,
 671 2005; J. Connolly, 2009) can also be employed in lieu of the simpler relations for more
 672 accurate predictions of seismic wave velocities in any given bulk composition (Stixrude
 673 & Lithgow-Bertelloni, 2011).

674 **6 Separating SPO from CPO in tomographic models: Application to** 675 **radial anisotropy beneath oceanic plates**

676 **6.1 Radial anisotropy beneath oceanic plates**

677 Within the context of seismic tomography, surface waves offer the capability to
 678 image upper-mantle structure providing an in-depth view of large-scale anisotropy.
 679 Surface wave tomography images positive radial anisotropy underneath oceanic basins
 680 ($V_{SH} > V_{SV}$), characterized by a layer of strong signatures lying in between $\sim 80 - 200$
 681 km depth, corresponding to the asthenosphere (e.g. J.-P. Montagner, 1985; Ekström &
 682 Dziewonski, 1998; Panning & Romanowicz, 2006; Nettles & Dziewoński, 2008b). The
 683 maximum positive vertical gradient of ξ^* , at ~ 80 km depth, independent of plate age,
 684 is a recurrent feature in these tomographic models. This has raised questions about
 685 the potential use of radial anisotropy as a marker of the lithosphere-asthenosphere
 686 boundary (LAB), which is expected on the contrary to deepen with plate age (Burgos
 687 et al., 2014; Beghein et al., 2019). The strong radial anisotropy in the asthenosphere
 688 is usually explained by geodynamic models including CPO evolution (Becker et al.,
 689 2006, 2008).

690 Across the oceanic lithosphere, plate-averaged radial anisotropy (*i.e.*, all points
 691 in the radial anisotropy models with the same plate age are averaged) displays modest

692 levels of about 1–3%. Several models have been proposed to explain these observa-
 693 tions. Hansen et al. (2016) and Hedjazian et al. (2017) suggest that CPO-related radial
 694 anisotropy developed below the ridge is subsequently frozen in the lithosphere, lead-
 695 ing to an age-independent signature. It has also been proposed quasi-laminated melt
 696 structures, preserved during lithospheric thickening, can also explain this frozen-in
 697 signature of anisotropy (e.g. Auer et al., 2015; Debayle et al., 2020). Hence SPO may
 698 also be a potential explanatory mechanism, and a substantial fraction of the observed
 699 lithospheric anisotropy may be due to small-scale isotropic heterogeneities (Wang et
 700 al., 2013; Kennett & Furumura, 2015).

701 The corroboration of the composite law in a 2-D complex medium prompted us
 702 to assess the discrepancy between a tomographic model and a CPO model of upper-
 703 mantle radial anisotropy underneath a mid-ocean ridge. In our hypothesis, this should
 704 commensurate to the extrinsic radial anisotropy due to the unresolved small-scales in
 705 seismic velocities.

706 6.2 The tomographic model

707 In conjunction with the pre-existing global V_{SV} model of the upper-mantle con-
 708 strained from Rayleigh wave data DR2012 (Debayle & Ricard, 2012), we adopt the
 709 recent global V_{SH} model CAM2016SH of Ho et al. (2016) to acquire a plate-averaged
 710 2-D profile of radial anisotropy associated with slow-spreading oceanic ridges.

711 The V_S models were reconstructed by independently inverting Love (for V_{SH}
 712 models) and Rayleigh (for V_{SV} models) waveforms up to the fifth overtone between
 713 the period range 50 – 250 s using an extension of the automated waveform inversion
 714 approach of Debayle (1999). We refer the reader to Debayle and Ricard (2012) and
 715 Ho et al. (2016) for a more detailed description of the inversion procedure.

716 From the V_{SV} and V_{SH} models of the upper-mantle, we compute the tomographic
 717 counterpart of radial anisotropy using $\xi^* = (V_{SH}/V_{SV})^2$. Here, we acknowledge that
 718 ξ^* is not directly inferred from simultaneous inversions of Love and Rayleigh data but
 719 is a rudimentary estimate from the two S -wave velocity models that may conceivably
 720 have different qualities. We view the following exercise as only a proof-of-concept and
 721 therefore the results should be interpreted with caution.

722 The depth distribution of ξ^* spanning from 35 – 400 km is shown in Figure 9
 723 (top panel). Positive radial anisotropy values ($\xi^* > 1$) are confined in the upper \sim
 724 200 km of the model domain which is in close agreement with previous studies (e.g.
 725 J.-P. Montagner, 1985; Ekström & Dziewonski, 1998; Panning & Romanowicz, 2006).
 726 Although the origin of anisotropy imaged in the asthenosphere is well-understood
 727 purely in terms of CPO, anisotropy observed in the lithosphere may be a combination
 728 of CPO and SPO (Wang et al., 2013). Here our task is to invoke the composite law
 729 to isolate SPO from CPO in this tomographic model with the help of a homogenized
 730 CPO model.

731 **6.3 The CPO model**

732 In this section, we re-interpret the results of Hedjazian et al. (2017) where they
 733 examined radial anisotropy profiles predicted from CPO models produced by plate-
 734 driven flows underneath a mid-ocean ridge. From their work, we borrowed two CPO
 735 models that correspond to a fast-developing CPO and a slow-developing CPO. The
 736 rate is dictated by the dimensionless grain boundary mobility parameter M which con-
 737 trols the kinetics of grain growth (and hence, the degree of dynamic recrystallization)
 738 (E. Kaminski et al., 2004). In the first case, a value of $M = 125$ constrained from
 739 laboratory experiments (Nicolas et al., 1973; Zhang & Karato, 1995) corresponding
 740 to CPO produced from uniform deformation and initially-random CPO was imposed
 741 (E. Kaminski et al., 2004). Subsequently, the second case considers a case where M
 742 = 10 (*i.e.*, slower CPO evolution) which also reproduces experimental results but in
 743 the case of an initially developed CPO (Boneh et al., 2015). Hedjazian et al. (2017)
 744 compared the CPO anisotropy directly with tomographic models. They concluded
 745 that the patterns of radial anisotropy predicted with the slow CPO evolution were
 746 in better agreement with tomographic models. We homogenize the two CPO models
 747 and obtain their long-wavelength effective equivalent, and again appraise the resulting
 748 profiles in comparison with tomographic observations.

749 **6.3.1 The intrinsic CPO mineralogical model**

750 2-D surface-driven mantle flows were acquired using the code `Fluidity` (Davies
 751 et al., 2011). In both models, upper-mantle deformation is governed by a composite
 752 dislocation and diffusion creep rheology following the implementation of Garel et al.

(2014). D-Rex was used to model CPO evolution. A complete description of the methodology can be found in Hedjazian et al. (2017).

Figure 9 displays the intrinsic radial anisotropy profiles ξ_{CPO} belonging to the fast-evolving CPO with reference D-Rex values $M = 125$ (model A) and the slow-evolving CPO with $M = 10$ (model B). Model A predicts a layer with strong levels of intrinsic radial anisotropy of about 10% ($\xi_{\text{CPO}} \approx 1.1$) at a depth of ~ 80 km starting at approximately 20 My. At about the same depth, tomographic models yield approximately 5% radial anisotropy (e.g. Panning & Romanowicz, 2006; Nettles & Dziewoński, 2008b; Burgos et al., 2014). Hence, it has been argued that model A overpredicts the observed level of large-scale anisotropy in the upper-mantle (Hedjazian et al., 2017). On the contrary, model B predicts modest levels of intrinsic radial anisotropy, about 5% ($\xi_{\text{CPO}} \approx 1.05$) across the oceanic lithosphere which is more consistent with tomographic observations.

6.3.2 The homogenized CPO model

Figure 9 now shows the effective intrinsic radial anisotropy profiles ξ_{CPO}^* of model A* and model B*. In both cases, the ensuing patterns of radial anisotropy are smoothed out as a result of homogenization. For instance, the apparent two-layered distribution of intrinsic radial anisotropy with depth (down to ~ 250 km) in model A vanishes after homogenization. The depth profile of effective intrinsic radial anisotropy as a result contain one layer of radial anisotropy centered at ~ 100 km depth, making it now compatible with tomographic models of the asthenosphere. Furthermore, it was implied that radial anisotropy predicted with typical laboratory-derived parameters exceeds tomographic observations. Here, we argue that it may also be the other way around. Due to finite-frequency effects and eventually limitations in resolution power, seismic tomography may underestimate the strength of intrinsic anisotropy, at least in the absence of small-scale isotropic heterogeneities. The level of radial anisotropy in models A and B are therefore larger than their homogenized/tomographic counterparts (models A* and B*). As opposed to common practice, the physical parameters used in CPO models of which are initially constrained by experimental data may need not be manually tuned, and perhaps that the action of varying such parameters to conform with tomographic observations deems unnecessary. We therefore conclude that direct visual comparison between a CPO model and a tomographic model could lead to wrong

785 interpretations, and that homogenization is necessary to have correct interpretations
786 of the CPO models.

787 **6.4 Deriving an SPO model**

788 The SPO models of Figure 9 (models C and D) can be estimated by using our
789 composite law in equation (31). The extrinsic radial anisotropy is obtained by simply
790 dividing the tomographic model of radial anisotropy by that of the homogenized CPO
791 model:

$$792 \quad \xi_{\text{SPO}}^* = \frac{\xi^*}{\xi_{\text{CPO}}^*}. \quad (37)$$

793 In this way, models C and D are obtained from models A* and B*, respectively.

794 Strong levels of positive extrinsic radial anisotropy near the ridge axis may be
795 due to the inability of surface waves to register vertical flow because of its limited
796 lateral resolution. Model D, associated with the slow-evolving CPO model B, is almost
797 devoid of SPO. This is expected since model B was tailored to fit seismic tomography
798 observations from CPO only. Based on our results, one should favor SPO model C
799 that corresponds to a fast-evolving CPO model. It displays positive extrinsic radial
800 anisotropy above 200 km depth. This is more consistent with the existence of lateral
801 fine-scale structures at the base of the lithosphere (e.g. Auer et al., 2015; Kennett &
802 Furumura, 2015).

803 **7 Conclusion**

804 Differentiating the relative contributions of CPO and SPO to the full effective
805 medium is not a simple, straightforward process. The tomographic operator (here ap-
806 proximated by \mathcal{H}) acts as a smoothing operator, and its inverse is highly non-unique.
807 It is therefore clearly impossible to separate the CPO and SPO contributions in a
808 tomographic model. One of the most logical courses of action is to compare tomo-
809 graphic models of anisotropy with existing micro-mechanical models of CPO evolution
810 (e.g. Becker et al., 2003, 2006; Ferreira et al., 2019). Here, we proposed a very simple
811 composite law that directly relates the separate contributions of CPO and SPO to the
812 full effective radial anisotropy ξ^* inferred from tomographic models:

$$813 \quad \xi^* = \xi_{\text{SPO}}^* \times \xi_{\text{CPO}}^*,$$

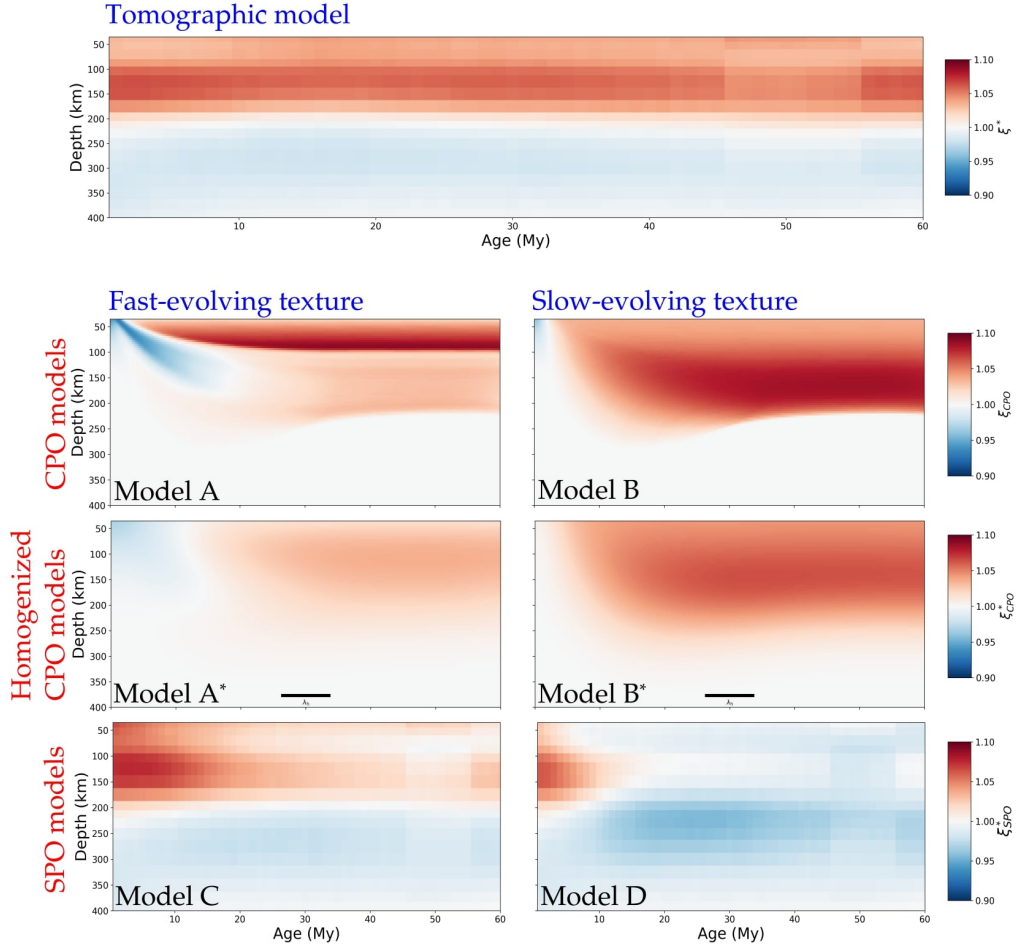


Figure 9. Plate-averaged radial anisotropy across the upper-mantle beneath oceanic basins with ages ranging between 0 and 80 Myrs obtained from a tomographic model (top panel), reference CPO models corresponding to fast and slow-evolving textures (models A and B), homogenized versions of model A (model A*) and of model B (model B*). Models C and D, respectively, are the extrinsic radial anisotropy profiles computed by dividing ξ^* of the tomographic model, by ξ_{CPO}^* of model A* and B*, using the composite law. Positive lithospheric radial anisotropy in model C implies the existence of horizontally-laminated structures. This is absent in model D which is expected since model B* is designed to fit observations.

814 which we have numerically verified using simple 2-D toy models of an intrinsically
 815 anisotropic and a heterogeneous mantle. Although our numerical experiments were
 816 mainly a proof-of-concept, comparing a CPO model directly to an existing tomographic
 817 model is unwarranted and we highly recommend homogenizing a CPO model as an
 818 intermediate step.

819 Acknowledgments

820 This work has been funded by the European Union Horizon 2020 research and
 821 innovation programme under grant agreement 716542. The computations were per-
 822 formed using the in-house **TRANSCALE** cluster situated in Lyon.

823 References

- 824 Agranier, A., Blichert-Toft, J., Graham, D., Debaille, V., Schiano, P., & Albarède,
 825 F. (2005). The spectra of isotopic heterogeneities along the mid-atlantic ridge.
 826 *Earth and Planetary Science Letters*, *238*(1-2), 96–109.
- 827 Alder, C., Bodin, T., Ricard, Y., Capdeville, Y., Debayle, E., & Montagner, J.
 828 (2017). Quantifying seismic anisotropy induced by small-scale chemical hetero-
 829 geneities. *Geophysical Journal International*, *211*(3), 1585–1600.
- 830 Allègre, C. J., & Turcotte, D. L. (1986). Implications of a two-component marble-
 831 cake mantle. *Nature*, *323*(6084), 123–127.
- 832 Auer, L., Becker, T. W., Boschi, L., & Schmerr, N. (2015). Thermal structure,
 833 radial anisotropy, and dynamics of oceanic boundary layers. *Geophysical Re-
 834 search Letters*, *42*(22), 9740–9749.
- 835 Backus, G. E. (1962). Long-wave elastic anisotropy produced by horizontal layering.
 836 *Journal of Geophysical Research*, *67*(11), 4427–4440.
- 837 Bakulin, A. (2003). Intrinsic and layer-induced vertical transverse isotropy. *Geo-
 838 physics*, *68*(5), 1708–1713.
- 839 Ballmer, M. D., Schmerr, N. C., Nakagawa, T., & Ritsema, J. (2015). Composi-
 840 tional mantle layering revealed by slab stagnation at \sim 1000-km depth. *Science
 841 Advances*, *1*(11), e1500815.
- 842 Becker, T. W., Chevrot, S., Schulte-Pelkum, V., & Blackman, D. K. (2006). Statis-
 843 tical properties of seismic anisotropy predicted by upper mantle geodynamic
 844 models. *Journal of Geophysical Research: Solid Earth*, *111*(B8).

- 845 Becker, T. W., Kellogg, J. B., Ekström, G., & OConnell, R. J. (2003). Compari-
846 son of azimuthal seismic anisotropy from surface waves and finite strain from
847 global mantle-circulation models. *Geophysical Journal International*, *155*(2),
848 696–714.
- 849 Becker, T. W., Kustowski, B., & Ekström, G. (2008). Radial seismic anisotropy as
850 a constraint for upper mantle rheology. *Earth and Planetary Science Letters*,
851 *267*(1-2), 213–227.
- 852 Beghein, C., Xing, Z., & Goes, S. (2019). Thermal nature and resolution of the
853 lithosphere–asthenosphere boundary under the pacific from surface waves.
854 *Geophysical Journal International*, *216*(2), 1441–1465.
- 855 Bodin, T., Capdeville, Y., Romanowicz, B., & Montagner, J.-P. (2015). Interpreting
856 radial anisotropy in global and regional tomographic models. In *The earth’s*
857 *heterogeneous mantle* (pp. 105–144). Springer.
- 858 Boneh, Y., Morales, L. F., Kaminski, E., & Skemer, P. (2015). Modeling olivine
859 cpo evolution with complex deformation histories: Implications for the in-
860 terpretation of seismic anisotropy in the mantle. *Geochemistry, Geophysics,*
861 *Geosystems*, *16*(10), 3436–3455.
- 862 Browaeys, J. T., & Chevrot, S. (2004). Decomposition of the elastic tensor and geo-
863 physical applications. *Geophysical Journal International*, *159*(2), 667–678.
- 864 Burgos, G., Montagner, J.-P., Beucler, E., Capdeville, Y., Mocquet, A., & Drilleau,
865 M. (2014). Oceanic lithosphere-asthenosphere boundary from surface wave
866 dispersion data. *Journal of Geophysical Research: Solid Earth*, *119*(2), 1079–
867 1093.
- 868 Bystricky, M., Kunze, K., Burlini, L., & Burg, J.-P. (2000). High shear strain of
869 olivine aggregates: Rheological and seismic consequences. *Science*, *290*(5496),
870 1564–1567.
- 871 Capdeville, Y., Guillot, L., & Marigo, J.-J. (2010). 2-d non-periodic homogenization
872 to upscale elastic media for p–sv waves. *Geophysical Journal International*,
873 *182*(2), 903–922.
- 874 Capdeville, Y., & Marigo, J.-J. (2007). Second order homogenization of the elas-
875 tic wave equation for non-periodic layered media. *Geophysical Journal Interna-*
876 *tional*, *170*(2), 823–838.
- 877 Capdeville, Y., & Métivier, L. (2018). Elastic full waveform inversion based on the

- 878 homogenization method: theoretical framework and 2-d numerical illustrations.
879 *Geophysical Journal International*, 213(2), 1093–1112.
- 880 Capdeville, Y., Stutzmann, E., Wang, N., & Montagner, J.-P. (2013). Residual ho-
881 mogenization for seismic forward and inverse problems in layered media. *Geo-*
882 *physical Journal International*, 194(1), 470–487.
- 883 Capdeville, Y., Zhao, M., & Cupillard, P. (2015). Fast fourier homogenization for
884 elastic wave propagation in complex media. *Wave Motion*, 54, 170–186.
- 885 Chang, S.-J., & Ferreira, A. M. (2019). Inference on water content in the mantle
886 transition zone near subducted slabs from anisotropy tomography. *Geochem-*
887 *istry, Geophysics, Geosystems*, 20(2), 1189–1201.
- 888 Chen, W.-P., & Brudzinski, M. R. (2003). Seismic anisotropy in the mantle transi-
889 tion zone beneath fiji-tonga. *Geophysical Research Letters*, 30(13).
- 890 Coltice, N., & Ricard, Y. (1999). Geochemical observations and one layer mantle
891 convection. *Earth and Planetary Science Letters*, 174(1-2), 125–137.
- 892 Connolly, J. (2009). The geodynamic equation of state: what and how. *Geochem-*
893 *istry, Geophysics, Geosystems*, 10(10).
- 894 Connolly, J. A. (2005). Computation of phase equilibria by linear programming: a
895 tool for geodynamic modeling and its application to subduction zone decarbon-
896 ation. *Earth and Planetary Science Letters*, 236(1-2), 524–541.
- 897 Crampin, S., & Booth, D. C. (1985). Shear-wave polarizations near the north ana-
898 tolian fault–ii. interpretation in terms of crack-induced anisotropy. *Geophysical*
899 *Journal International*, 83(1), 75–92.
- 900 Davies, D. R., Wilson, C. R., & Kramer, S. C. (2011). Fluidity: A fully unstructured
901 anisotropic adaptive mesh computational modeling framework for geodynam-
902 ics. *Geochemistry, Geophysics, Geosystems*, 12(6).
- 903 Debayle, E. (1999). Sv-wave azimuthal anisotropy in the australian upper mantle:
904 preliminary results from automated rayleigh waveform inversion. *Geophysical*
905 *Journal International*, 137(3), 747–754.
- 906 Debayle, E., Bodin, T., Durand, S., & Ricard, Y. (2020). Seismic evidence for par-
907 tial melt below tectonic plates. *Nature*, 586(7830), 555–559.
- 908 Debayle, E., & Kennett, B. (2000). Anisotropy in the australasian upper mantle
909 from love and rayleigh waveform inversion. *Earth and Planetary Science Let-*
910 *ters*, 184(1), 339–351.

- 911 Debayle, E., & Ricard, Y. (2012). A global shear velocity model of the upper man-
 912 tle from fundamental and higher rayleigh mode measurements. *Journal of Geo-*
 913 *physical Research: Solid Earth*, 117(B10).
- 914 Debayle, E., & Ricard, Y. (2013). Seismic observations of large-scale deformation
 915 at the bottom of fast-moving plates. *Earth and Planetary Science Letters*, 376,
 916 165–177.
- 917 Ekström, G., & Dziewonski, A. M. (1998). The unique anisotropy of the pacific up-
 918 per mantle. *Nature*, 394(6689), 168–172.
- 919 Estey, L. H., & Douglas, B. J. (1986). Upper mantle anisotropy: a preliminary
 920 model. *Journal of Geophysical Research: Solid Earth*, 91(B11), 11393–11406.
- 921 Faccenda, M., Ferreira, A. M., Tisato, N., Lithgow-Bertelloni, C., Stixrude, L., &
 922 Pennacchioni, G. (2019). Extrinsic elastic anisotropy in a compositionally
 923 heterogeneous earth’s mantle. *Journal of Geophysical Research: Solid Earth*,
 924 124(2), 1671–1687.
- 925 Ferreira, A. M., Faccenda, M., Sturgeon, W., Chang, S.-J., & Schardong, L. (2019).
 926 Ubiquitous lower-mantle anisotropy beneath subduction zones. *Nature Geo-*
 927 *science*, 12(4), 301–306.
- 928 Fichtner, A., Kennett, B. L., Igel, H., & Bunge, H.-P. (2010). Full waveform to-
 929 mography for radially anisotropic structure: new insights into present and past
 930 states of the australasian upper mantle. *Earth and Planetary Science Letters*,
 931 290(3-4), 270–280.
- 932 Fichtner, A., Kennett, B. L., & Trampert, J. (2013). Separating intrinsic and appar-
 933 ent anisotropy. *Physics of the Earth and Planetary Interiors*, 219, 11–20.
- 934 Garel, F., Goes, S., Davies, D., Davies, J. H., Kramer, S. C., & Wilson, C. R.
 935 (2014). Interaction of subducted slabs with the mantle transition-zone: A
 936 regime diagram from 2-d thermo-mechanical models with a mobile trench and
 937 an overriding plate. *Geochemistry, Geophysics, Geosystems*, 15(5), 1739–1765.
- 938 Guillot, L., Capdeville, Y., & Marigo, J.-J. (2010). 2-d non-periodic homogeniza-
 939 tion of the elastic wave equation: Sh case. *Geophysical Journal International*,
 940 182(3), 1438–1454.
- 941 Gung, Y., Panning, M., & Romanowicz, B. (2003). Global anisotropy and the thick-
 942 ness of continents. *Nature*, 422(6933), 707–711.
- 943 Hansen, L. N., Faccenda, M., & Warren, J. M. (2021). A review of mech-

- 944 anisms generating seismic anisotropy in the upper mantle. *Physics of*
 945 *the Earth and Planetary Interiors*, 106662. Retrieved from [https://](https://www.sciencedirect.com/science/article/pii/S0031920121000200)
 946 www.sciencedirect.com/science/article/pii/S0031920121000200 doi:
 947 <https://doi.org/10.1016/j.pepi.2021.106662>
- 948 Hansen, L. N., Qi, C., & Warren, J. M. (2016). Olivine anisotropy suggests guten-
 949 berg discontinuity is not the base of the lithosphere. *Proceedings of the Na-*
 950 *tional Academy of Sciences*, 113(38), 10503–10506.
- 951 Hedjazian, N., Capdeville, Y., & Thomas, B. (2021). Multiscale seismic imaging
 952 with inverse homogenization. *Geophysical Journal International*.
- 953 Hedjazian, N., Garel, F., Davies, D. R., & Kaminski, E. (2017). Age-independent
 954 seismic anisotropy under oceanic plates explained by strain history in the
 955 asthenosphere. *Earth and Planetary Science Letters*, 460, 135–142.
- 956 Ho, T., Priestley, K., & Debayle, E. (2016). A global horizontal shear velocity model
 957 of the upper mantle from multimode love wave measurements. *Geophysical*
 958 *journal international*, 207(1), 542–561.
- 959 Hofmann, A. W. (1988). Chemical differentiation of the earth: the relationship be-
 960 tween mantle, continental crust, and oceanic crust. *Earth and Planetary Sci-*
 961 *ence Letters*, 90(3), 297–314.
- 962 Kaminski, É., & Ribe, N. M. (2002). Timescales for the evolution of seismic
 963 anisotropy in mantle flow. *Geochemistry, Geophysics, Geosystems*, 3(8), 1–
 964 17.
- 965 Kaminski, E., Ribe, N. M., & Browaeys, J. T. (2004). D-rex, a program for calcu-
 966 lation of seismic anisotropy due to crystal lattice preferred orientation in the
 967 convective upper mantle. *Geophysical Journal International*, 158(2), 744–752.
- 968 Kendall, J., & Silver, P. (1998). Investigating causes of d'' anisotropy. *The core-*
 969 *mantle boundary region*, 28, 97–118.
- 970 Kennett, B., & Furumura, T. (2015). Toward the reconciliation of seismological and
 971 petrological perspectives on oceanic lithosphere heterogeneity. *Geochemistry,*
 972 *Geophysics, Geosystems*, 16(9), 3129–3141.
- 973 Kumazawa, M., & Anderson, O. L. (1969). Elastic moduli, pressure derivatives, and
 974 temperature derivatives of single-crystal olivine and single-crystal forsterite.
 975 *Journal of Geophysical Research*, 74(25), 5961–5972.
- 976 Lev, E., & Hager, B. H. (2008). Prediction of anisotropy from flow models: A com-

- 977 comparison of three methods. *Geochemistry, Geophysics, Geosystems*, 9(7).
- 978 Long, M. D., & Becker, T. W. (2010). Mantle dynamics and seismic anisotropy.
- 979 *Earth and Planetary Science Letters*, 297(3-4), 341–354.
- 980 Love, A. E. H. (1906). *A treatise on the mathematical theory of elasticity, by ach*
- 981 *love*. The University Press.
- 982 Maupin, V., & Park, J. (2015). 1.09theory and observationsseismic anisotropy. *Trea-*
- 983 *tise on Geophysics*, 277–305.
- 984 Maupin, V., Park, J., Romanowicz, B., & Dziewonski, A. (2007). Theory and obser-
- 985 vationswave propagation in anisotropic media. *Seismology and the Structure of*
- 986 *the Earth. Treatise on Geophysics*, 1, 289–321.
- 987 McKenzie, D. (1979). Finite deformation during fluid flow. *Geophysical Journal In-*
- 988 *ternational*, 58(3), 689–715.
- 989 McNamara, A. K., van Keken, P. E., & Karato, S. (2002). Development of
- 990 anisotropic structure by solid-state convection in the earths lower mantle.
- 991 *Nature*, 416(6878), 310–314.
- 992 Meade, C., Silver, P. G., & Kaneshima, S. (1995). Laboratory and seismological
- 993 observations of lower mantle isotropy. *Geophysical Research Letters*, 22(10),
- 994 1293–1296.
- 995 Montagner, J., & Nataf, H. (1988). Vectorial tomography. part i: Theory. *Geophysi-*
- 996 *cal Journal International*, 94, 295–307.
- 997 Montagner, J.-P. (1985). Seismic anisotropy of the pacific ocean inferred from long-
- 998 period surface waves dispersion. *Physics of the earth and planetary interiors*,
- 999 38(1), 28–50.
- 1000 Montagner, J.-P. (2007). Upper mantle structure: Global isotropic and anisotropic
- 1001 elastic tomography. *Treatise on geophysics*, 1, 559–589.
- 1002 Montagner, J.-P., & Nataf, H.-C. (1986). A simple method for inverting the az-
- 1003 imuthal anisotropy of surface waves. *Journal of Geophysical Research: Solid*
- 1004 *Earth*, 91(B1), 511–520.
- 1005 Nettles, M., & Dziewoński, A. M. (2008a). Radially anisotropic shear velocity struc-
- 1006 ture of the upper mantle globally and beneath north america. *Journal of Geo-*
- 1007 *physical Research: Solid Earth*, 113(B2).
- 1008 Nettles, M., & Dziewoński, A. M. (2008b). Radially anisotropic shear velocity struc-
- 1009 ture of the upper mantle globally and beneath north america. *Journal of Geo-*

- 1010 *physical Research: Solid Earth*, 113(B2).
- 1011 Nicolas, A., Boudier, F., & Boullier, A. (1973). Mechanisms of flow in naturally and
1012 experimentally deformed peridotites. *American Journal of Science*, 273(10),
1013 853–876.
- 1014 Nicolas, A., & Christensen, N. I. (1987). Formation of anisotropy in upper mantle
1015 peridotites—a review. *Composition, structure and dynamics of the lithosphere-
1016 asthenosphere system*, 16, 111–123.
- 1017 Obrebski, M., Kiselev, S., Vinnik, L., & Montagner, J.-P. (2010). Anisotropic strat-
1018 ification beneath africa from joint inversion of sks and p receiver functions.
1019 *Journal of Geophysical Research: Solid Earth*, 115(B9).
- 1020 Panning, M., & Romanowicz, B. (2006). A three-dimensional radially anisotropic
1021 model of shear velocity in the whole mantle. *Geophysical Journal Interna-
1022 tional*, 167(1), 361–379.
- 1023 Plomerová, J., Kouba, D., & Babuška, V. (2002). Mapping the lithosphere–
1024 asthenosphere boundary through changes in surface-wave anisotropy. *Tectono-
1025 physics*, 358(1-4), 175–185.
- 1026 Press, W. H., Teukolsky, S. A., Flannery, B. P., & Vetterling, W. T. (1992). *Numer-
1027 ical recipes in fortran 77: volume 1, volume 1 of fortran numerical recipes: the
1028 art of scientific computing*. Cambridge university press.
- 1029 Ricard, Y., & Bercovici, D. (2009). A continuum theory of grain size evolution and
1030 damage. *Journal of Geophysical Research: Solid Earth*, 114(B1).
- 1031 Stixrude, L., & Jeanloz, R. (2015). Constraints on seismic models from other
1032 disciplines—constraints from mineral physics on seismological models.
- 1033 Stixrude, L., & Lithgow-Bertelloni, C. (2011). Thermodynamics of mantle minerals-
1034 ii. phase equilibria. *Geophysical Journal International*, 184(3), 1180–1213.
- 1035 Sturgeon, W., Ferreira, A. M., Faccenda, M., Chang, S.-J., & Schardong, L. (2019).
1036 On the origin of radial anisotropy near subducted slabs in the midmantle. *Geo-
1037 chemistry, Geophysics, Geosystems*, 20(11), 5105–5125.
- 1038 Tauzin, B., Bodin, T., Debayle, E., Perrillat, J.-P., & Reynard, B. (2016). Multi-
1039 mode conversion imaging of the subducted gorda and juan de fuca plates
1040 below the north american continent. *Earth and Planetary Science Letters*, 440,
1041 135–146.
- 1042 Tauzin, B., & Ricard, Y. (2014). Seismically deduced thermodynamics phase di-

- 1043 agrams for the mantle transition zone. *Earth and Planetary Science Letters*,
1044 401, 337–346.
- 1045 Tkalčić, H., Pasyanos, M. E., Rodgers, A. J., Gök, R., Walter, W., & Al-Amri, A.
1046 (2006). A multistep approach for joint modeling of surface wave dispersion
1047 and teleseismic receiver functions: Implications for lithospheric structure of the
1048 arabian peninsula. *Journal of Geophysical Research: Solid Earth*, 111(B11).
- 1049 Tommasi, A., Mainprice, D., Canova, G., & Chastel, Y. (2000). Viscoplastic self-
1050 consistent and equilibrium-based modeling of olivine lattice preferred orien-
1051 tations: Implications for the upper mantle seismic anisotropy. *Journal of*
1052 *Geophysical Research: Solid Earth*, 105(B4), 7893–7908.
- 1053 Trampert, J., & van Heijst, H. J. (2002). Global azimuthal anisotropy in the transi-
1054 tion zone. *Science*, 296(5571), 1297–1299.
- 1055 Wang, N., Montagner, J.-P., Fichtner, A., & Capdeville, Y. (2013). Intrinsic versus
1056 extrinsic seismic anisotropy: The radial anisotropy in reference earth models.
1057 *Geophysical Research Letters*, 40(16), 4284–4288.
- 1058 Wookey, J., & Kendall, J.-M. (2004). Evidence of midmantle anisotropy from shear
1059 wave splitting and the influence of shear-coupled p waves. *Journal of Geophys-
1060 ical Research: Solid Earth*, 109(B7).
- 1061 Xu, W., Lithgow-Bertelloni, C., Stixrude, L., & Ritsema, J. (2008). The effect of
1062 bulk composition and temperature on mantle seismic structure. *Earth and*
1063 *Planetary Science Letters*, 275(1-2), 70–79.
- 1064 Zhang, S., & Karato, S.-i. (1995). Lattice preferred orientation of olivine aggregates
1065 deformed in simple shear. *Nature*, 375(6534), 774.